Ullal Pranav Nayak

Efeito da estampagem incremental de ponto simples na microestrutura e propriedades mecânicas do alumínio e do aço

Effect of single point incremental forming on the microstructure and mechanical properties of aluminum and steel

Universidade de Aveiro

Ano 2015/2016

Departamento de Quimica

Ullal Pranav Nayak

Efeito da estampagem incremental de ponto simples na microestrutura e propriedades mecânicas do alumínio e do aço

Effect of single point incremental forming on the microstructure and mechanical properties of aluminum and steel

Dissertação apresentada á Universidade de Aveiro para cumprimento dos requisitos necessário á obtenção do grau de Mestre em Ciência e Engenharia de Materiais/Funcionalized Advanced Materials and Engineering, realizada sob a orientação cientifica do Dr. Augusto Luís Barros Lopes, Professor Auxiliar do Departamento de Engenharia de Materiais e Cerâmica da Universidade de Aveiro.

Dissertation presented to the University of Aveiro for the requirement of partial fulfilment of Masters of Science degree in Materials Science and Engineering/Functionalized Advanced Materials and Engineering under the supervision of Dr. Augusto Luís Barros Lopes, Auxiliary Professor in the Department of Materials and Ceramic Engineering of the University of Aveiro.

Jury:

President	Prof. Ana Margarida Madeira Viegas de Barros Timmons, University of Aveiro
	Prof. Manuel Fernando Gonçalves Vieira, University of Porto
	Prof. Augusto Luís Barros Lopes, University of Aveiro

Palavras-Chave   Estampagem incremental, SPIF, comportamento mecânico, textura cristalográfica, microestrutura de deslocações.

Resumo   Neste trabalho foi investigado o efeito da deformação plástica por estampagem incremental de ponto simples (SPIF) na textura cristalográfica, estrutura de deslocações e propriedades mecânicas de chapas de alumínio, aço com baixo teor em carbono e aço de fase dupla.

Foram realizados ensaios de tração nos materiais iniciais para caracterizar as suas propriedades mecânicas. Além disso, foram realizadas análises por difração de eletrões retrodispersados (EBSD), observações por microscopia eletrónica de transmissão (TEM) e cálculos utilizando o modelo viscoplástico autoconsistente para caracterizar a influência da textura cristalográfica e da microestrutura no comportamento mecânico dos materiais. Foram também realizadas medidas de deformação e de espessura, bem como ensaios de microdureza nos materiais deformados por SPIF.

Em todos os materiais, a textura cristalográfica inicial revelou-se muito estável durante o processo de SPIF e foi observado um acentuado aumento da densidade de deslocações bem como o desenvolvimento de células equiaxiais de deslocações durante a deformação de ambos os aços. No entanto, na chapa de alumínio, não foram observadas alterações significativas da microestrutura inicial de laminagem. Em todos os materiais foi observado um bom acordo entre a espessura das peças obtidas por SPIF e o valor previsto pela lei do seno.

Keywords   Incremental forming, SPIF, mechanical behavior, crystallographic texture, dislocation microstructure.

Abstract   In this work, was investigated the effect of the plastic deformation by single point incremental forming (SPIF) on the crystallographic texture, dislocation structure and mechanical properties of aluminum, low carbon steel and dual phase steel sheets.

Tensile tests were conducted on the initial materials to characterize their mechanical behavior. Furthermore, electron backscattering diffraction (EBSD), transmission electron microscopy (TEM) observations and calculations using a polycrystalline viscoplastic self-consistent (VPSC) model were carried to characterize the influence of the crystallographic texture and microstructure on the mechanical behavior of the materials. Strain and thickness measurements and microhardness tests were also conducted on the SPIF deformed materials.

The initial crystallographic texture was very stable during the SPIF of all materials and a strong increase of dislocation density and the development of equiaxed dislocation cell structure was observed during the deformation of both steels. However, for the aluminum sheet, no major change was observed on the initial rolling microstructure. For all materials, it was observed a good agreement between the thickness of the SPIF pieces and the value predicted by the sin law.

Table of Contents

List of Figures

List of Tables

List of Abbreviations

2D	2-dimensional
3D	3-dimensional
AHSS	Advanced high strength steels
ALCOA	Aluminum Company of America
ASTM	American Society for Testing and Materials
BCC	Body centered cubic
CAD	Computer aided design
CAM	Computer aided manufacturing
CISF	Conventional incremental sheet forming
CNC	Computer numerical control
CP	Complex phase
DP	Dual phase
EBSD	Electron backscattering diffraction
FB	Ferritic-bainitic steel
FCC	Face centered cubic
FFLD	Fracture forming limit diagram
FLC	Forming limit curve
FLD	Forming limit diagram
GDP	Gross domestic product
HDD	Hard disk drive
HISF	Hybrid incremental sheet forming
ISF	Incremental sheet forming
LC	Low-carbon
MS	Martensitic steel
ND	Normal direction
POSCO	Pohang Iron and Steel Company
PVC	Poly-vinyl chloride
RD	Rolling direction

SEM	Scanning electron microscope
SPIF	Single point incremental forming
SPIHF	Single point incremental hydro forming
TD	Transverse direction
TEM	Transmission electron microscope
TPIF	Two point incremental forming
TPIFFD	Two point incremental forming with full die
TPIFPD	Two point incremental forming with partial die
TRIP	Transformation induced plasticity
TWIP	Twin induced plasticity
USA	United States of America
VPSC	Viscoplastic self-consistent

List of Symbols

(a, b, c)	Crystallographic frame
(X, Y, Z)	Specimen frame
$(\varepsilon_1\ \varepsilon_2)$	Principal strain space
$(\varphi_1, \Phi, \varphi_2)$	Euler angles
$\dot{\gamma}_c^s$	Reference shear strain rate (s^{-1})
$\dot{\gamma}^s$	Shear strain rate (s^{-1})
d_1 and d_2	Diameter of the circles measured perpendicular and parallel to the direction of tool movement, respectively
d_1^o and d_2^o	Initial values of d_1 and d_2, respectively
l_o, w_o and t_o	Initial length, width and thickness of the sheet, respectively
m^s	Schmid factor
$\overline{R}$	Normal anisotropy coefficient
R_θ	Anisotropic coefficient with respect to the angle, θ
α'	Average interaction intensity between dislocations
ε_{11}	Length true strain
ε_{22}	Width true strain
ε_{33}	Thickness true strain
$\tilde{\tau}$	Average shear stress (MPa)
τ_o	Frictional stress for dislocation movement (MPa)
$< M^{-1} >$	Mean value of the inverse Taylor factor
$<M>$	Average Taylor factor
$<\varepsilon>$	Average strain
$<\sigma>$	Average stress (MPa)
A_o	Initial cross-section area (mm^2)
b	Burgers vector of the dislocations
d	Average length of the diagonal of the indentation (mm)
F	Applied force (N)

G	Shear modulus (GPa)
HV	Hardness value
l, w and t	Final length, width and thickness of the sheet, respectively
ln	Natural logarithm
M	Taylor factor
R	Anisotropic coefficient/Lankford parameter
s	Slip system
t	Final sheet thickness (mm)
t_o	Initial sheet thickness (mm)
α	Amplitude of strain path change
β	Incremental forming/draw angle (°)
β_{max}	Maximum forming/draw angle (°)
Δl	Change in length (mm)
ΔR	Planar anisotropy coefficient
Δz	Incremental step-down size (mm)
ε	True strain
$\varepsilon_1{}^{max}$	Maximum major true strain
ε_f	True strain experienced by ferrite grains
ε_u	Total uniform strain
η	Reciprocal strain rate sensitivity coefficient
θ	Loading angle
λ	Angle between applied stress and slip direction (°)
ρ	Dislocation density (m^{-2})
σ	True stress (MPa)
σ_{max}	Maximum stress (MPa)
σ_o	Yield stress (MPa)
$\tau_c{}^s$	Critically resolved shear stress (MPa)
τ^s	Shear stress (MPa)
Φ	Angle between applied stress and slip plane normal (°)

1. Introduction

Historically, the development of a civilization depends on its ability to select, produce and use materials for their needs. Nowadays, different materials are used for various applications ranging from housing, to medical care, to communication, etc. Before selecting any material, one has to consider several factors such as availability, cost, ease of manufacture and the suitable chemical and physical properties. Metals form an integral part of several industries such as automobile, aerospace, construction and millions of tons of metals are processed every year through various forming process.

The shaping operations can be categorized into bulk and sheet forming. Conventional forming processes such as deep drawing, stamping, punching etc. make use dies and punches. These are manufactured depending on the shape and dimensions of the components to be produced. However, these conventional processes are only suitable for mass-production of components due to its high initial investment.

Recent diversification in customer demand has forced the industry to produce smaller batches at the lowest possible price. These requirements have justified an increase interest on incremental forming techniques, such as single point incremental forming (SPIF), where a sheet metal is deformed using a simple tool without the help of a die. This type of processes are particularly well adapted for the production of parts with complex shapes for different industries by rapid prototyping . In recent years, many different materials such as aluminum, titanium, PVC, etc. have been processed using SPIF.

Phenomena that can limit the quality of the products, such as springback, sheet thinning and localized plastic strain, obtained by traditional sheet forming operations can also be observed in SPIF. Despite all the research, the physical mechanism that governs the plastic deformation during the SPIF process is not fully understood and needs to be further investigated.

The main objective of this work was to study the effect of plastic deformation by SPIF on the crystallographic texture, dislocation structure and mechanical properties of aluminum, low carbon steel and dual phase steel sheets.

The current thesis is organized in six chapters, the Introduction being the first one.

Chapter 2 presents a bibliographic review of the material properties, applications and the studies conducted on them. This chapter also covers the main aspects of forming, plastic deformation, crystallographic texture, dislocation structures and their influence on the mechanical behavior of metals.

Chapter 3 describes the initial material, experimental work and the techniques used for the material characterization.

The results and discussions are presented in chapter 4.

Finally, the conclusions and proposal for future work have been described in chapters 5 and 6, respectively.

2. Literature Review

2.1. Sheet Metal Forming Processes

Since approximately 4000 B.C., mankind has been producing metal components using different tools and techniques. Today, metal forming serves as a backbone for the modern manufacturing industry. Every year, hundreds of millions of tons of metals undergo metal forming process throughout the world, contributing to 15-20% of the gross domestic product (GDP) of industrialized nations (Kumar 2015).

It is usual to classify the metal shaping processes in four major groups: casting, plastic forming, cutting and joining. Plastic forming can be further categorized into two types: bulk forming and sheet forming. Bulk forming consists of deforming the material in the form of a billet, rod or slab. In the second type of forming processes, the initial material is used in the form of sheets and do not present significant variation in the thickness during the shaping operation (Wagoner 2002).

Conventional forming processes such as stamping, deep drawing, punching, etc. makes use of dies and punches which are manufactured according to the shape and dimensions of the component. Due to very high initial investment to produce these dies, the process is very expensive and it is suitable only for mass production of components. In recent years, the needs of the customer were so diversified that the lot size had to be reduced. Due to that, the cost of manufacturing the forming tools needed to be reduced as well. This paved way for developing production techniques for small batches. One idea was to create a deformation of sheets using a simple tool without the help of a die. This idea of 'dieless forming' was already patented by Leszak in the United States in 1967 (Leszak 1967), even before it was technically viable. After that, there was a significant interest in processes where the sheet metal is deformed plastically in a small zone, enabling a fast and flexible production of complex parts (Müller 1998). This method, called incremental sheet forming (ISF), has now become very attractive due to the advances in manufacturing technology especially in the field of numerical control and automation. Jesweit et al., provided a comprehensive review of the process development covering most aspects of incremental sheet forming (Jeswiet 2005). Single

point incremental forming (SPIF) is one such process of incremental sheet forming which has been receiving great attention from the scientific community in the past few years (Jeswiet 2005) (Benedetti 2015).

2.1.1. Incremental Sheet Forming

The term incremental forming is a generic term used for a variety of processes that are characterized by the fact that at any given time, only a small part of the product is being deformed by the application of a step-by-step incremental feed to a deforming tool (Tisza 2012). The ISF process can be defined as a manufacturing process done usually with a small sized tool in continuous contact with a small zone of the sheet that is deformed without any dedicated die (Jeswiet 2005). In conventional sheet forming processes, dedicated tools are necessary which are complex to produce and hence, expensive. In incremental forming technique, only a deforming tool is required.

In the most common ISF processes, there are four basic elements: a metallic sheet, a blank holder/edge, a deforming tool and a computer control system. The blank edge is clamped and the sheet is deformed usually by a hemispherical tool, whose path is defined by the computer control system as shown in Figure 1. The incremental step-down size (Δz) affects the surface quality and the processing time. A decrease of the step-down size corresponds to an increase of the surface quality of the obtained piece, as shown in Figure 2, but also an increase in the processing time. Feed rate is the speed with which the forming tool moves around the deformation area. Forming angle (β) is defined as the angle between the normal of the un-deformed sheet metal and the deformed sheet wall. The maximum forming angle (β_{max}) is the highest forming angle possible to use without the occurrence of failure. This parameter is usually used as a measure of formability of the material during the ISF process (Ham 2006) (Ham M 2007).
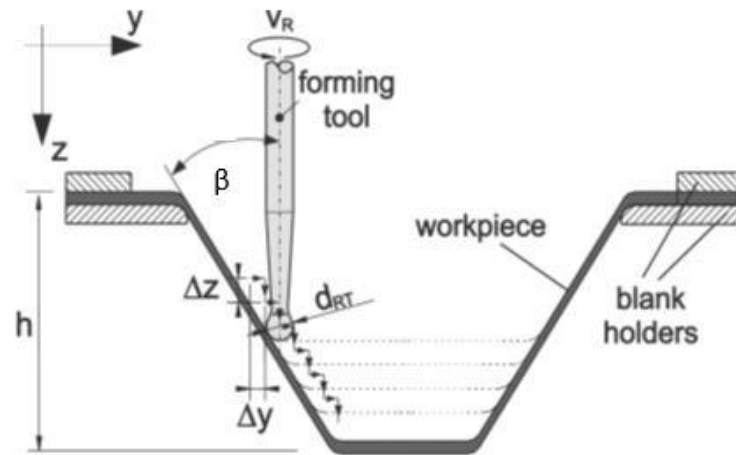
Figure 1: Basic principle of incremental forming (Tisza 2012). β is the forming angle and Δz is the incremental step-down size.

ISF, that can be seen as combination of stretch forming and metal spinning processes, is able of produce 3D complex shapes (Kumar 2015) and has received a significant increase in the research activity during the last years (Jeswiet J. 2001) (Jeswiet 2005) (Leach 2001) (Kitazawa 1997) (Powell 1992), (Benedetti 2015), (Milutinović 2014).
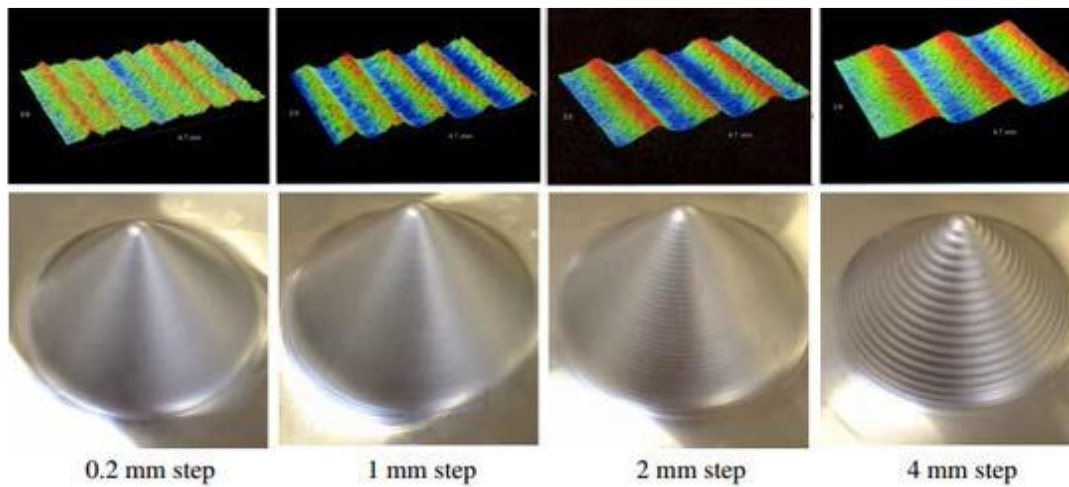
Figure 2: Surface roughness in pieces produced by ISF with different incremental step-down sizes (M. B. Silva 2008).

2.1.2. Classification of Incremental Sheet Forming

Incremental forming may be classified based on forming methods, forming path, applied tools, part geometry, etc. However, the most common classification is done based on forming methods. They can be categorized into conventional incremental sheet forming (CISF) and hybrid incremental sheet forming (HISF).

2.1.2.1. Conventional Incremental Sheet Forming

In CISF processes, the sheet of metal is progressively deformed with the help of a hemispherical or ballpoint tool, resulting in a localized plastic deformation. The tool moves over the surface of the sheet whose path is defined by computer controlled system, resulting in the final product. These process can be further classified into:

- Single point incremental forming (SPIF): It is also called negative dieless forming. In this, only one tool moves over the surface, as shown in Figure 3;
- Two point incremental forming (TPIF): Also known as positive dieless forming, uses two tools: one deformation tool and another supporting tool move over the surface of the sheet, as shown in Figure 4.
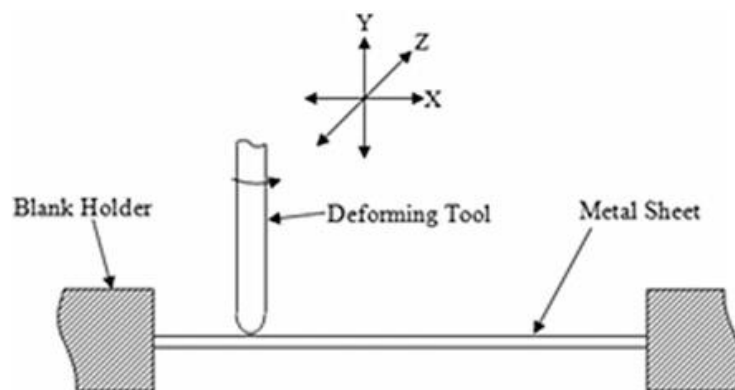
Figure 3: Single point incremental forming (SPIF) (Kumar 2015).
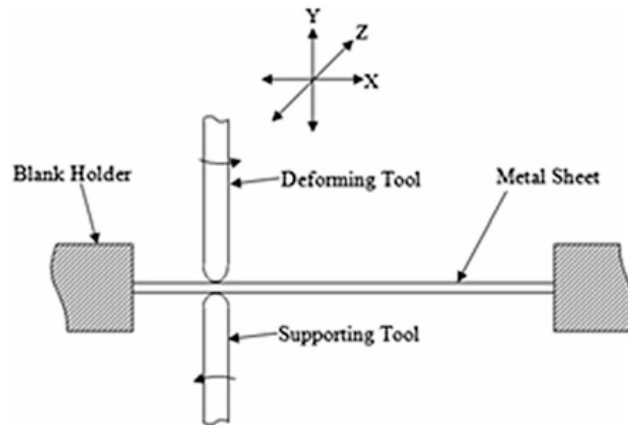
Figure 4: Two point incremental forming (TPIF) (Kumar 2015).

2.1.2.2. Hybrid Incremental Sheet Forming

The HISF processes are modified versions of CISF. In addition to the deformation tool moving over one of the surfaces of the sheet, the other side of the sheet is supported by pressurized hydraulic fluid, partial die or a full die to get the desired size and shape. Depending of the selected support, the hybrid incremental forming processes are classified into:

- Single point incremental hydro-forming (SPIHF): In this type of hybrid incremental forming, the deformation tool moves over the surface of the sheet while the other side is supported by a pressurized hydraulic fluid, as shown in Figure 5;
- TPIF with partial die (TPIFPD): The desired shape is obtained with the help of the deformation tool which moves over one side of the sheet while the other side is supported by a partial die, as shown in Figure 6;
- TPIF with full die (TPIFFD): The partial die is replaced by the full die to get the desired shape and size, as shown in Figure 7.
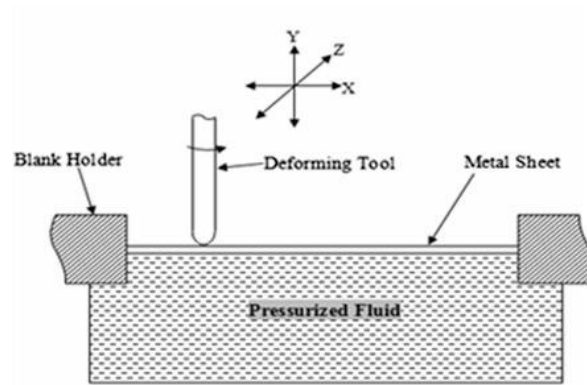
Figure 5: Single point incremental hydro-forming (SPIHF) (Kumar 2015).
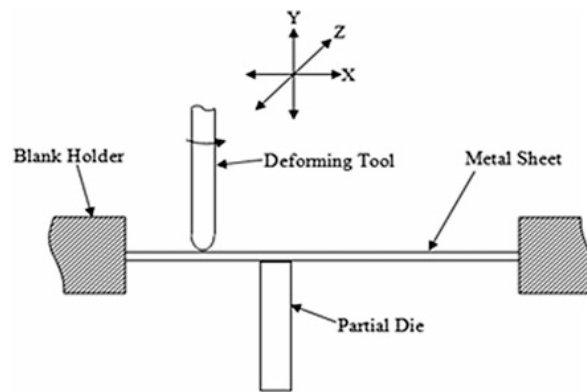
Figure 6: Two point incremental forming with partial die (TPIFPD) (Kumar 2015).
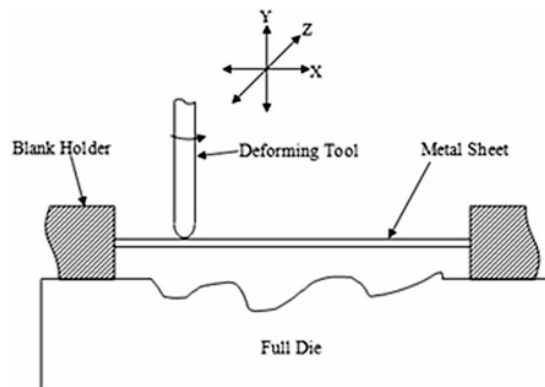
Figure 7: Two point incremental forming with full die (TPIFFD) (Kumar 2015).

Further classification on ISF can be done based on the forming method depending on whether it is a single-step or a multi-step process (Echrif 2011). Taking the geometry of the formed sheet into account, the ISF processes can be classified as symmetric and asymmetric (Tisza 2012).

2.1.3. Single Point Incremental Forming

2.1.3.1. The Process

Single point incremental forming is a simple, yet innovative, process to produce both axisymmetric and non-axisymmetric parts. It uses simple tools such as, a cylindrical metal tool with a spherical tip, to deform the sheet metal and does not require any die to accomplish the process. Due to this, the forming forces are much smaller compared to other conventional sheet forming processes. It has been shown by several studies that SPIF can be performed with a standard three-axis computer numerical control (CNC) mill (Jeswiet J. 2001) (Leach 2001) (Filice 2002). The basic components involved in SPIF are shown in Figure 8. The schematic representation of the cross-section view of SPIF is shown in Figure 9.
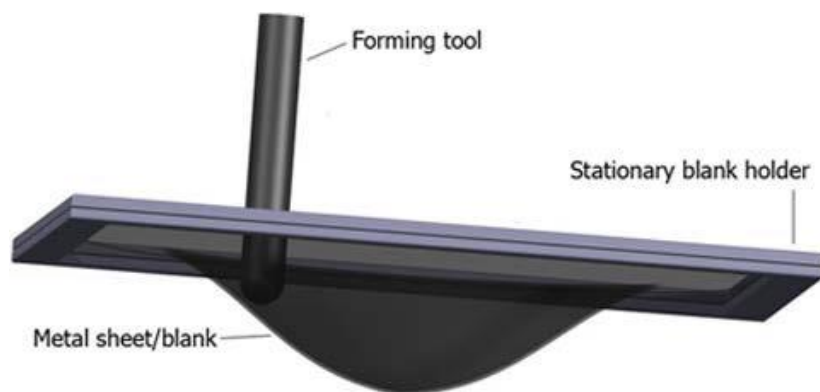
Figure 8: Components in SPIF (Torrão 2013).
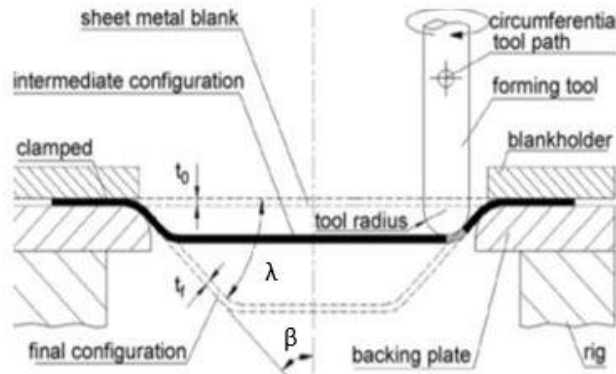
Figure 9: Schematic representation of SPIF (P. A. Martins 2008).

By applying pressure on the surface of the sheet using the tool, the deformation is accomplished. The metal sheet is restrained by the blank holder to avoid displacement and flow of material into the forming area. The backing plate supports the sheet and its opening defines the forming area of the deformation tool. The computerized system controls the tool path and no back up die is used to support the back surface of the metal sheet during the process. Figure 10 illustrates an exemplificative path taken by the forming tool. The tool path can be unidirectional or bi-directional, although it is mentioned that the unidirectional tool path might lead to twisting in the part produced (Jadhav 2004). The thickness of the obtained piece wall (t) can be related with the forming angle (β) through the sine law (Jeswiet 2005):

$$t = t_0 \sin(\beta) \tag{1}$$

where, t_0 is the initial thickness of the sheet.
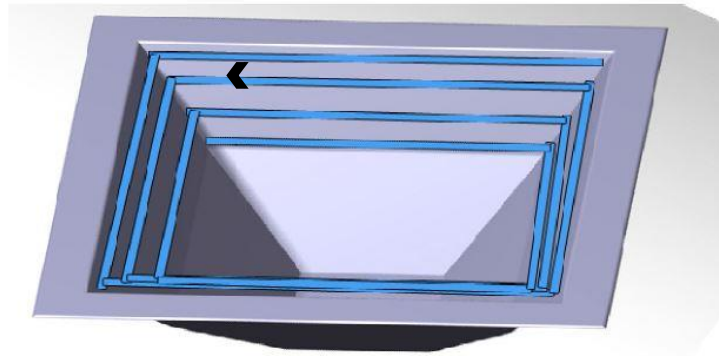
Figure 10: Example of unidirectional path followed by the SPIF tool (M. Martins 2011).

2.1.3.2. Advantages and Disadvantages

As a result of several studies conducted on SPIF, some advantages and disadvantages have been pointed out by many authors (Jeswiet 2005) (J. M. Allwood 2004). The main advantage lies in the fact that it does not require any positive or negative dies, thus saving a lot of time and financial investment in the production of these dies. The parts can be formed directly from computer aided design (CAD) data files with minimal specialized tooling while the design changes can be accounted for easily and quickly, making the process flexible. The deforming tool can be controlled entirely by a conventional CNC machine. The small plastic zone and the incremental nature of the process result in increased formability, making it easier to deform sheets with low formability. Finally, the entire operation is quiet and the applied loads are much smaller. The major disadvantage of this process is the longer forming time compared to other forming process, resulting in the production of smaller batches in the same timeframe. Also, a multistep process is needed to produce the right angles that cannot be done in one step. Depending on the material, the springback phenomena during the forming process can give rise to undesired distortions of the final shape (Meier 2009) and must be accounted for.

2.1.3.3. Applications

SPIF has a vast field of applications such as in the aerospace and automobile industries or fields such as health care (Milutinović 2014) (J. M. Allwood 2004). With the help of CAD/CAM software, various geometries can be produced and due to its versatility, it can handle different kinds of metals such as steel, aluminum, composite and polymeric materials (P. A. Martins 2009) (M. B. Silva 2010) (Franzen 2009) (Jesweit 2005). Some of the different geometries that can be produced using SPIF are shown in Figure 11.

| Five lobe shape | Faceted cone | Truncated pyramid |

Figure 11: Examples of geometries produced by SPIF (Jeswiet 2005) (M. Martins 2011).

In the area of rapid prototyping, SPIF is of major use as it has the capability of attaining functional parts such prostheses for the medical industry. A good example was presented by Duflou et al., (J. R. Duflou 2005) (Verbert 2008) who produced a cranial implant from the model of a patient's skull.
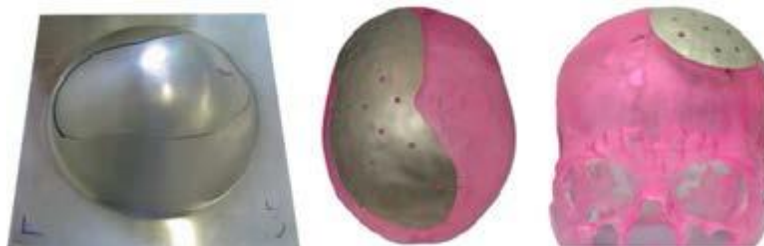
Figure 12: Cranial implant obtained by SPIF (J. R. Duflou 2005).

By employing reverse engineering, it is possible to produce replacements for discontinued parts. Other areas of products where SPIF is applicable are cellular phone, hard disk drives and sensors.

2.1.4. Formability in SPIF process

Incremental sheet forming is characterized by an increase in formability compared to conventional methods (Jeswiet 2005) (P. A. Martins 2008) (Fratini 2004). The governing mode of deformation which leads to this increase, has been a subject of controversy (M. B. Silva 2008) (Emmens 2007). Some have claimed that the deformation is mainly due to shearing rather than stretching whereas others have claimed the opposite (Y. H. Kim 2002) (T. J. Kim 2000) (Jackson 2009) (J. M. Allwood 2007).

Recent research has shown that the formability in SPIF is in very close correlation with the forming angle (β). From the sine law (eq. 1), increasing the forming angle corresponds to a decrease in the wall thickness and at a particular point (that defines a maximum forming angle, β_{max}), it will reach its minimum before undergoing fracture. Thus, the forming angle can be used to characterize the formability of the material during the SPIF process (Tisza 2012). However, the use of β_{max} gives only a rough approximation as the deformation mechanisms in SPIF are much more complex and formability cannot be defined by a single parameter (P. A. Martins 2008) (Tisza 2012) (Jeswiet 2005). As the process is affected by many parameters, a benchmark method was proposed by Micari (Micari 2004): using a truncated cone with a height of 40 mm and a base diameter of 72 mm as shown in Figure 13. Tests are performed at various cone angles until fracture, which is defined as tearing in the specimen wall. Table 1 shows the β_{max} value for the given initial thickness of different materials.
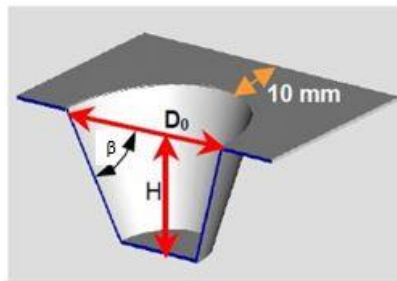
Figure 13: Benchmark specimen for testing forming parameters (Jeswiet 2005).

Table 1: Maximum forming angle (β_{max}) for different initial sheet thickness (t_o) and materials.

Material	β_{max} (°)	t_o (mm)	Reference
Aluminum 1050-O	67.5°	1.21	Filice (Filice 2002)
Aluminum 6114–T4	60°	1.0	Micari (Micari 2004)
Aluminum 3003 – O	78.1°	2.1	Jeswiet (Jeswiet 2005)
Aluminum 3003 – O	72.1°	1.3	Jeswiet (Jeswiet 2005)
Aluminum 3003 – O	71°	1.21	Jeswiet (Jeswiet 2005)
Aluminum 3003 – O	67°	0.93	Jeswiet (Jeswiet 2005)
DC04, mild steel	65°	1.0	Hirt (Hirt 2004)

Considering the complexity of the plastic deformation mechanisms involved in SPIF, theoretical prediction of formability is very difficult and hence forming limit diagrams (FLD) is the more common solution. These diagrams are an important tool to decide if a material with a particular thickness can be used in the forming operation to produce a piece without defects due to fracture or plastic instabilities. The forming limit diagrams have usually a V-shaped, as shown by the dashed lines in Figure 14. Nowadays, tests methods, such as Nakajima (Nakazima 1967) or Marciniak (Marciniak 1965) tests, are available to determine the FLD of conventional forming processes. Incremental sheet forming is characterized by local deformation modes which determine a forming limit curve with a negative slope for positive minor strains (Filice 2002) (Kumar 2015).
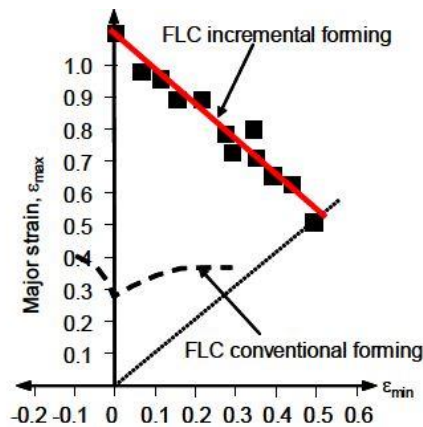
Figure 14: Typical forming limit diagram for conventional and incremental forming. FLC – forming limit curve (Jeswiet 2005).

Martins et.al (P. A. Martins 2008) performed experiments on 1 mm thickness aluminum AA1050-H111 sheets by varying the forming angle and found that plastic deformation occurs due to uniform thinning until fracture (Figure 15) without any experimental evidence of localized necking before fracture. In fact, necks are unable to grow in SPIF due to the small plastic deformation zone in contact with incremental forming tool. Even if the conditions for localized necking could be met at the small plastic deformation zone, as the surrounding material experiences relatively lower stresses, its growth would be inhibited (P. A. Martins 2008) (M. Martins 2011). This means that conventional FLDs are not able to describe the failure in SPIF. Instead, fracture forming limit diagrams (FFLDs) are usually employed in SPIF (M. B. Silva 2008) (Benedetti 2015).
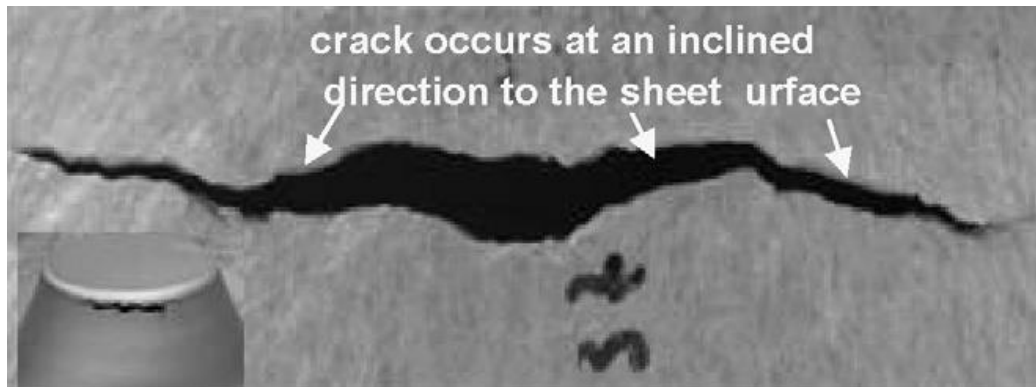
Figure 15: Experimental evidence of SPIF being limited by fracture without necking (P. A. Martins 2008).

Tisza (Tisza 2012) successfully determined both sides of the FLD in incremental forming (Figure 16) using a modified version of the conventional Marciniak test (Marciniak 1965). In this study, he concluded that the formability in incremental forming increases with the increase of the initial sheet thickness. Similar conclusions were drawn by Hirt et.al (Hirt 2004) who performed experiments with a mild steel sheet with different thickness.
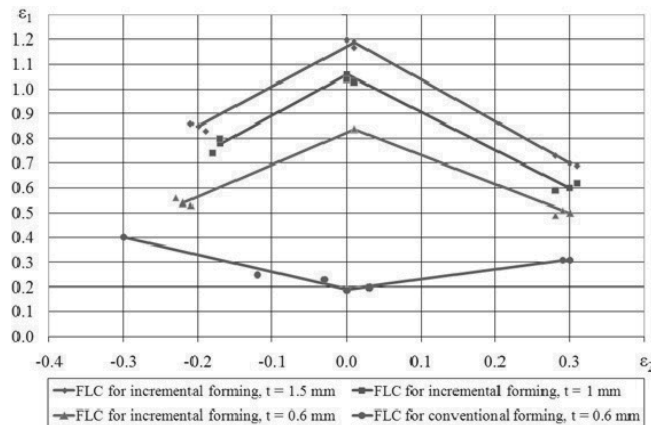
Figure 16: Comparison of FLD for conventional and incremental forming for aluminum 1050 sheet (Tisza 2012).

There have been several other studies centered on the formability in incremental forming. Kim and Yang suggested a multi-pass technique to improve formability by assuming an occurrence of shear deformation in the material (T. J. Kim 2000). This was also suggested by Duflou et.al to avoid damage localization. Emphasis was given on the control of the force to improve formability (J. R. Duflou 2008). Ambrogio et.al (Ambrogio 2006) and Duflou et.al (Duflou J. 2007) also suggested forming forces as a parameter to predict failure. Ambrogio et.al (Ambrogio G. 2008) have shown that the formability is enhanced when the sheet metals are deformed in warm conditions and that the effect of the tool diameter is negligible in comparison with the temperature and the step-down size. Kim and Park observed that as the feed rate decreases, the formability increases (Y. H. Kim 2002). Hussain et.al did extensive research on several materials to show how some material properties, such as strain hardening exponent, tensile and yield strength, anisotropy etc., influence the SPIF formability (Hussain 2009).

Ham and Jeswiet (Ham 2006) reported that the parameters involved in the process such as sheet thickness, step-down value, size of the forming tool and the speed of deformation all affect the formability of ISF. Micari (Micari 2004) conducted tests on 1mm thick AA1050-0 sheets with a cone configuration as shown in Figure 13 and concluded that the formability decreased as the step-down size increases. This was further observed by Hagan and Jeswiet (Hagan 2004). The next

figure shows the FLD_o (maximum major true strain, ε_1^{max}), for different step sizes for AA1050-0 for a tool diameter of 12mm performed by Micari (Micari 2004).
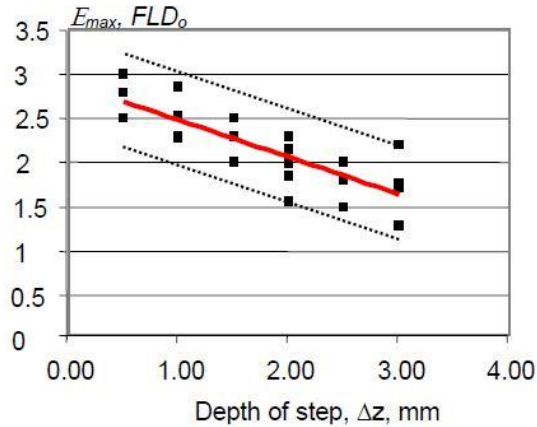
Figure 17: FLD_o values for different SPIF step-down sizes of aluminum 1050-O. The upper and lower bounds for a tool diameter of 12mm are represented (Micari 2004).

Micari (Micari 2004) also studied the effect the spindle angular speed and the forming tool diameter. By increasing the angular speed, local heating of the sheet will take place, which increases the formability. The negative aspect of this is that the wear of the tool will occur at a faster rate. The forming tool diameter is also an important processing parameter: tool with a small radius concentrates the strain in a small deformation zone while a larger radius tool tends to distribute it over a wider area. Increasing the tool radius will decrease formability as the process becomes similar to a stamping process (Jeswiet 2005) (Micari 2004). Hirt et.al (Hirt G. 2002) found out that the formability greatly increased by decreasing the tool radius from 30mm to 6mm. The influence of anisotropy on formability was investigated by Kim and Park (Y. H. Kim 2002) who concluded that, when small diameter tools are used, the formability differs with the direction with respect to the rolling direction of the metallic sheet.

Although many experiments have been performed in the past by several researchers, a consensus has not yet been reached regarding the exact deformation mechanism in SPIF which leads to increased formability. Emmens and Boogaard (Emmens 2007) have given a brief overview suggesting the possible mechanisms that lead to the increase in formability in incremental forming

such as a combination of stretching with shear forces, bending or normal forces, non-proportional or cyclic deformation paths, too small deformation zones and hydrostatic compressive stresses. Other mechanisms such as restriction of neck growth and the effect of hydrostatic pressure have also been mentioned in the literature (Emmens 2007) (Hirt G. 2002) (P. A. Martins 2008).

2.2. Materials

Over the years, SPIF has been used on many different materials such as aluminum, poly-vinyl chloride (PVC), steels, magnesium, titanium, brass, copper, etc. (Ambrogio G. 2008) (Ham 2006) (Hussain 2009) (Jesweit 2005) (Franzen 2009).

2.2.1. Aluminum

Aluminum is one of the most commonly used non-ferrous metals in applications which require reduced weight, such as the aerospace and automotive sector. Due to the need for fuel economy and weight saving, it has been playing an important role in the development of lightweight fuel-efficient transportation systems. With a density one-third that of steel, excellent ductility and corrosion resistance, pure aluminum can be modified by alloying and processing, giving it improved mechanical properties for several industries.

2.2.2. Steel

Steel is one of the most important engineering material, mainly due to its unique combination of strength, toughness and ductility. These properties justify its use in construction,

equipment and components, automobile industry, etc. It has become such an essential part of our society that the extent of consumption of steel is considered a key economic indicator for assessing the development of a country.

Steel is an alloy of iron and carbon that is usually categorized based on the carbon amount, as presented in next the table.

Table 2: Categorization of steels based on the carbon content.

Type	Carbon Content (wt. %)
Low-carbon steel	<0.3
Medium-carbon steel	0.3 - 0.7
High-carbon steel	0.7 - 2.0

Depending of the composition and processing, a wide variety of metallurgical structures with different properties can be produced. In addition to carbon, other common alloying elements are manganese, nickel, molybdenum, vanadium, chromium, etc.

2.2.2.1. Advanced High Strength Steels

Advanced high strength steels (AHSS) are a relatively recent technological advancement in steel production. These materials show an improved combination of strength, ductility, toughness and fatigue properties as a result of a careful selection of chemical composition and processing conditions. The AHSS steels includes the martensitic (MS), dual phase (DP), complex phase (CP), ferritic-bainitic (FB), transformation induced plasticity (TRIP) and twinning induced plasticity (TWIP) steels.
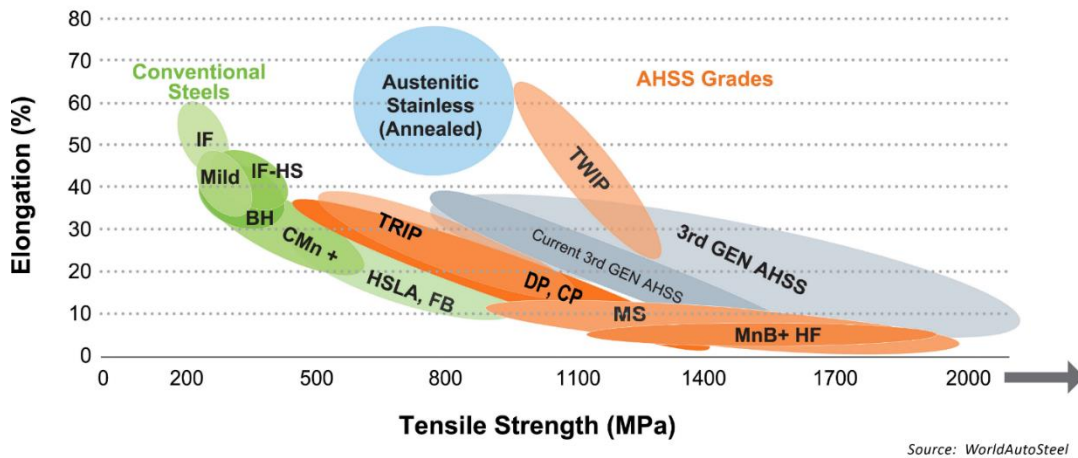
Figure 18: Typical tensile strength and elongation presented by AHSS and conventional steels (WorldAutoSteel 2014).

Between these materials, DP steels are one of the most important type of AHSS due to their excellent combination of strength, ductility and price. The microstructure is predominantly composed by ferrite and martensite (Figure 19). The hard martensite particles provide substantial strengthening while the ductile ferrite matrix gives good formability. This unique combination of properties of DP steels allows to produce both thin and high strength components for many applications, such as for the automotive industry (Federici 2005).
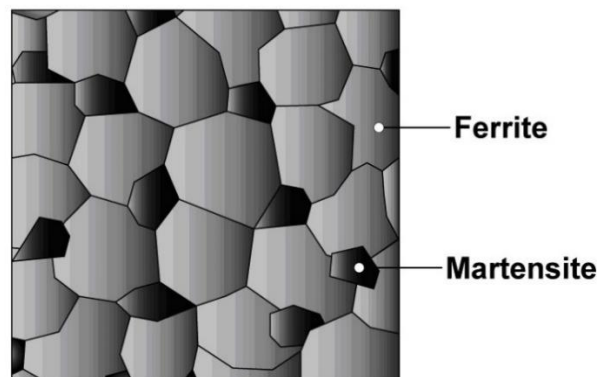
Figure 19: Schematic microstructure of DP steel (WorldAutoSteel 2014).

2.3. Plastic Deformation of Metallic Materials

2.3.1. Plastic Deformation Mechanisms

Plastic deformation occurs when the load applied is enough to prevent the material to recover its original shape after unload. Usually, plastic deformation at room temperature takes place through non-diffusive mechanisms such as slipping and twinning. Slip is usually seen in materials with high stacking fault energy such as aluminum whereas twin occurs in materials with low stacking fault energies such as brass (R. E. Smallman 1964) (Karaman 2000) (Abbaschian 2008).

Slip takes place by the movement and multiplication of dislocations along planes and directions (slip systems) of the crystal lattice with the highest atomic density, producing the movement of a portion of the crystal over the other part, as a result of an applied shear stress (τ^s). In face centered cubic (FCC) materials such as aluminum, these planes and directions correspond to {1 1 1} and <1 1 0>, respectively. In body centered cubic (BCC) crystals, such as iron, slip can occur at any one of the planes {1 1 0}, {1 1 2} and {1 2 3} along the most closed packed direction, <1 1 1> (R. E. Smallman 1964) (R. E. Smallman 2007).
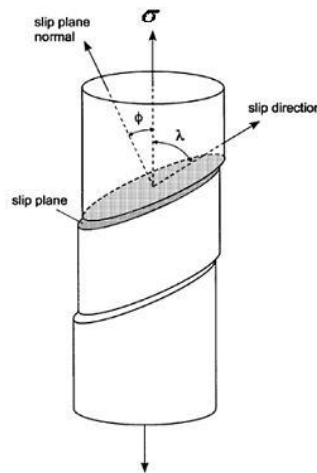
Figure 20: Slip in a single crystal (Dieter 1988).

The activation of a slip system (s) occurs when the shear stress on this slip system (τ^s) reaches a critical value τ_c^s (critically resolved shear stress), i.e.:

$$\begin{cases} \tau^s = \tau_c^s \rightarrow \text{slip system s is active} \\ \tau^s < \tau_c^s \rightarrow \text{slip system s is latent} \end{cases} \tag{2}$$

If σ is the tensile stress applied to the crystal and Φ and λ are the angles between the applied stress direction and, respectively, the normal of the slip plane and the slip direction:

$$\tau^s = \sigma \cos(\phi^s) \cos(\lambda^s) \tag{3}$$

The product $\cos(\phi^s) \cos(\lambda^s)$ is called the Schmid factor, m^s (Schmid 1924)

The value τ_c depends on the dislocation density and the frictional stress for movement of dislocation trough the following equation:

$$\tau_c = \tau_o + \alpha' \, Gb\sqrt{\rho} \tag{4}$$

where α' is the average interaction intensity between the dislocations, G is the shear modulus and b is the Burgers vector of the dislocations (Schmid 1924).

During the plastic deformation, dislocations are accumulated inside the grains and, after a certain amount of strain, they tend to organize themselves into structures (dislocation cells) whose shape depends upon the number of activated slip systems (Figure 21). When one or two slip systems are activated, the development of one or two families, respectively, of dislocation walls parallel to the slip planes with highest activity takes place. When more than two slip systems are activated, equiaxial dislocation cells are observed. With the increase of strain, the density of dislocations increase resulting in the decrease in size of the dislocation cells and an increase in the relative crystallographic misorientations between neighboring cells. The degree of organization of dislocations depend on the dislocation mobility. In materials where the dislocations have high mobility, a well-defined dislocation cell structure can be observed whereas lower dislocation mobility leads to a more homogeneous distribution of dislocations and no well-defined cells are observed inside the grains (Kuhlmann-Wilsdorf 1989) (Rauch 2004) (Dutta 2011).
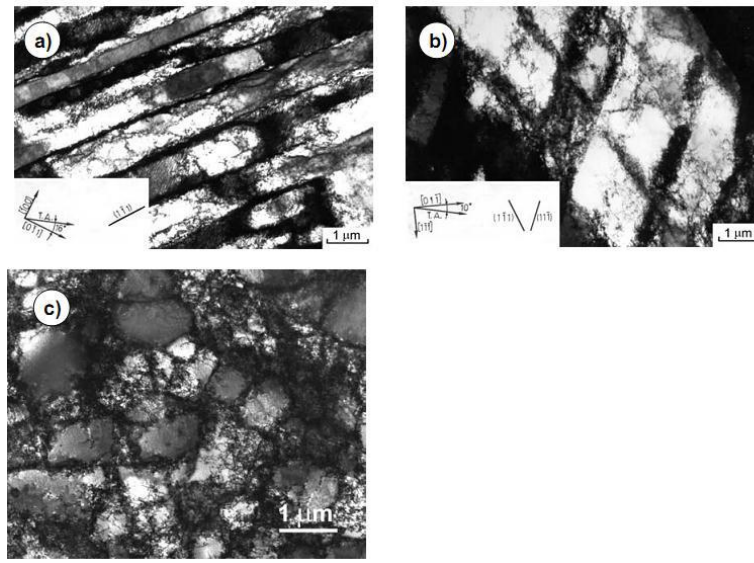
Figure 21: TEM dislocation microstructure of a) one b) two families of parallel dislocation walls and c) equiaxial dislocation cells (Lopes 2001).

2.3.2. Crystallographic Texture

The crystallographic texture is the preferential orientation of the grains in a polycrystalline material. This preferential orientation of grains occurs during previous heat treatment or plastic deformation operations and is many times responsible for an anisotropic behavior of the material.

The most widespread form of representing the crystallographic texture is by pole figures which is a stereographic projection of the distribution density of the given {hkl} crystallographic plane normals. For cubic materials, it is necessary at least two different pole figures to define completely the crystallographic texture.
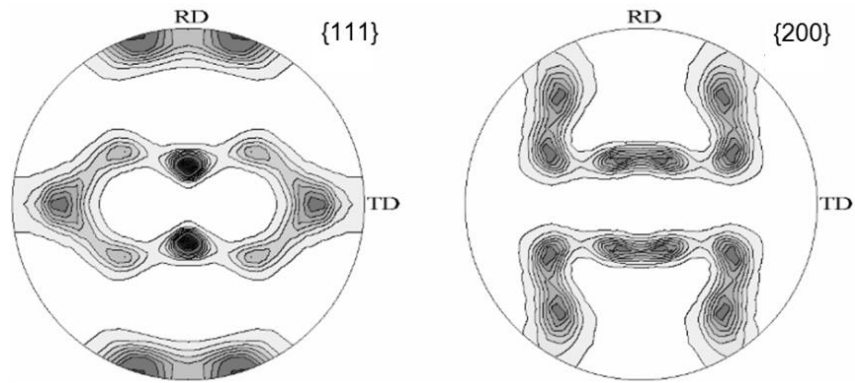
Figure 22: Typical {111} and {200} pole figures of aluminum after conventional rolling. RD-rolling direction (Kudrathon 2010).

In case of sheets, the crystallographic planes {hkl} parallel to the sheet plane and directions <uvw> parallel to RD can be used to identify the preferential crystallographic orientation of the grains. For example, the typical rolling components of aluminum are the copper {112}<111>, S{123}<634> and Brass {011}<211> (Engler 2009).

Other representation of the crystallographic orientation of the grains in the polycrystals is the three consecutive rotations (Euler angles: φ_1, Φ, φ_2) that transform the crystallographic frame (a, b, c) to the specimen frame (X, Y, Z) (Bunge 1982) (Suwas 2014).
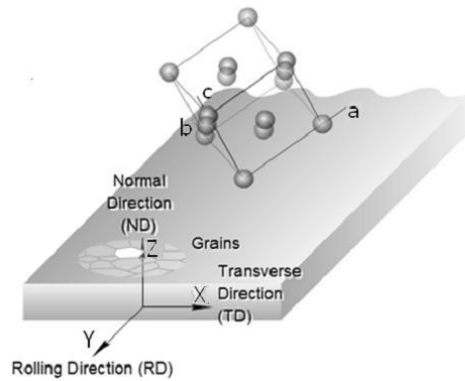
Figure 23: Definition of crystal axis (a=[100], b=[010] and c=[001]) and macroscopic specimen axis for a sheet (X, Y, Z) (Dutta 2011).

Taking into account the orientation of each individual grain (g = (φ_1, Φ, φ_2)), the texture of the polycrystal can be represented in Euler space by 3D iso-surfaces as shown in Figure 24 (a).

24

However, as this representation is complex to analyze, the texture of the polycrystal is usually represented by 2D representations of Euler space at constant φ_2, as shown in Figure 24 (b) and Figure 25.
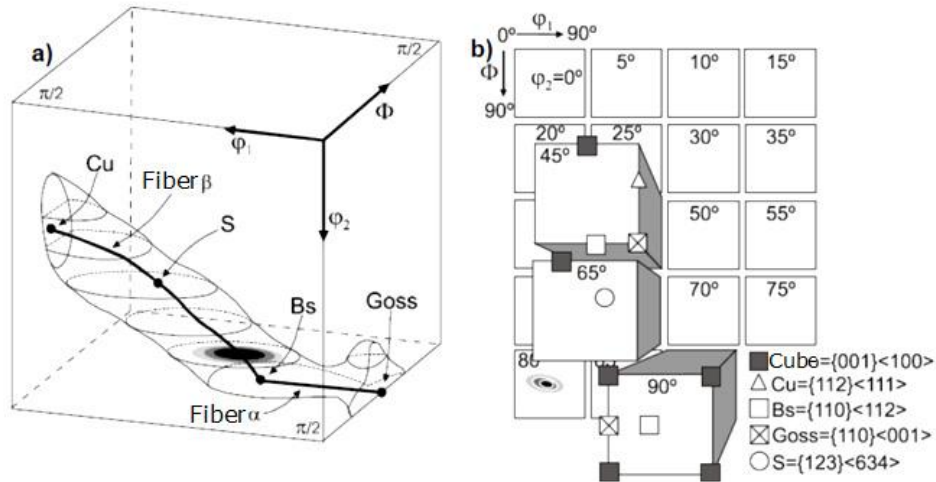
Figure 24: Crystallographic texture representation in Euler's space a) three-dimensional representation; b) two-dimensional representation of sections with constant values of φ_2 (Bunge 1982).
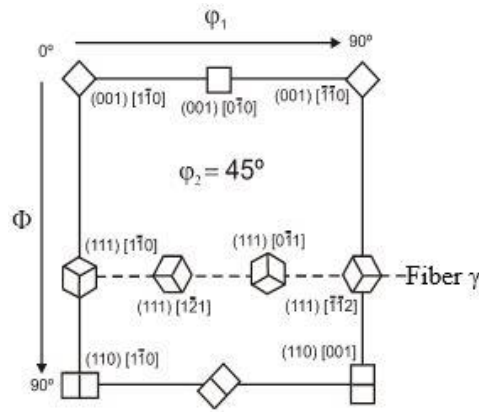
Figure 25: $\varphi_2=45°$ section of Euler space representation of some main crystallographic texture components of steel (Suwas 2014).

2.3.3. Polycrystalline models of plastic deformation

Polycrystalline materials consist of several grains oriented in different crystallographic directions that have mutual interactions which affect the mechanical behavior of each crystal and, therefore, of the material. These interactions between the grains leads to local accommodation processes resulting in differences between macroscopic and microscopic imposed stress or strain states. Depending on how these accommodation processes are considered, different models have been proposed to correlate the mechanical behavior in the polycrystal and in each grain (R. A. Lebensohn 1993) (Kudrathon 2010) (Dutta 2011).

2.3.3.1. Sachs Model

The Sachs model (Sachs 1928) assumes that there is no interaction between the neighboring grains in the polycrystal and hence, it considers that the stress imposed upon each grain is uniform and equal to the macroscopic stress, as in monocrystals. The plastic deformation is accommodated in each grain by the activation of the slip system with the highest Schmid factor (Schmid 1924).

In this case, taking into account the different crystallographic orientations of the grains, the entire behavior of the polycrystal can be represented by the average behavior of the crystals (Zaoui 1990).

$$\sigma = < M^{-1} > \tilde{\tau} \tag{5}$$

where, $< M^{-1} >$ is the mean value of the inverse Taylor factor and $\tilde{\tau}$ is the average shear stress acting on the crystals.

2.3.3.2. Taylor Model

The Taylor model assumes that all the grains in the polycrystalline material undergo the same homogeneous strain as the polycrystal. This requires the activation of at least five

independent slip systems. The activated slip systems are the ones that minimize the deformation energy, e.g. (Taylor 1938):

$$(W_{int})_{min} = (\sum_{s=1}^{5} \tau_c^s |\gamma^s|)_{min} \tag{6}$$

where, $(W_{int})_{min}$ represents the minimum internal work necessary to plastically deform the polycrystalline material, τ_c^s and γ^s represent the critically resolved shear stress and the shear strain in the slip system, s, respectively.

The limitation of this model lies in the fact that this condition can occur for different sets of five independent slip systems giving rise to ambiguity in the selection.

Assuming that the critical shear stress value is same for all slip systems ($\tau = \tau_c^s$):

$$\frac{\sigma}{\tau} = \frac{(\sum_{s=1}^{S} |\gamma^s|)_{min}}{\varepsilon} = M \tag{7}$$

where, σ and ε are the macroscopic imposed stress and strain respectively. M is the Taylor factor which takes into account the orientation of the grains with respect to the stress applied. If all the grains are considered, the Taylor factor should be replaced by the average Taylor factor <M> and the expression can be re-written as:

$$\sigma = <M> \tilde{\tau} \tag{8}$$

2.3.3.3. Viscoplastic Model

The viscoplastic model, considers that the shear strain rate, $\dot{\gamma}^s$ in each slip system is dependent on the resolved shear stress τ^s through the equation (Molinari 1987) (Austin 2011):

$$\dot{\gamma}^s = \dot{\gamma}_c^s \left(\frac{\tau^s}{\tau_c^s}\right)^\eta \tag{9}$$

In the above equation, the $\dot{\gamma}_c^s$ and the τ_c^s are, respectively, the reference shear strain rate and the critical resolved shear stress of the slip system (s) and η is the reciprocal strain rate sensitivity coefficient of the material.

This model assumes that all slip system are activated during the plastic deformation (with different activity) and is usually combined with self-consistent conditions:

$$E = <\varepsilon> \tag{10}$$

$$\Sigma = <\sigma> \tag{11}$$

where E and Σ are, respectively the macroscopic stress and strain applied to the polycrystal and $<\varepsilon>$ and $<\sigma>$ represent the average strain and stress on the individual crystals.

2.3.4. Mechanical Behavior

The mechanical behavior of the polycrystal depends upon the individual contribution of the grains, considering their crystallographic orientations and the local interactions between the neighboring grains. Besides that, other parameters such as prestrain value, amplitude of strain path change and strain rate also effect the mechanical behavior of the material.

2.3.4.1. Anisotropy

Anisotropy is the change of a property with the direction of the material. If the property is the strain, the anisotropy can be characterized by an anisotropic coefficient (R), also called Lankford parameter, given by:

$$R = \frac{\varepsilon_{22}}{\varepsilon_{33}} \tag{12}$$

where ε_{22} and ε_{33} are the true strains in the width and thickness directions, respectively, (see Figure 26) and calculated through the following equations:

$$\varepsilon_{22} = \ln\left(\frac{w}{w_o}\right) \tag{13}$$

$$\varepsilon_{33} = \ln\left(\frac{t}{t_o}\right) \tag{14}$$

with w_o and t_o representing the initial width and thickness and w and t representing the final width and thickness of the sheet specimen, respectively.
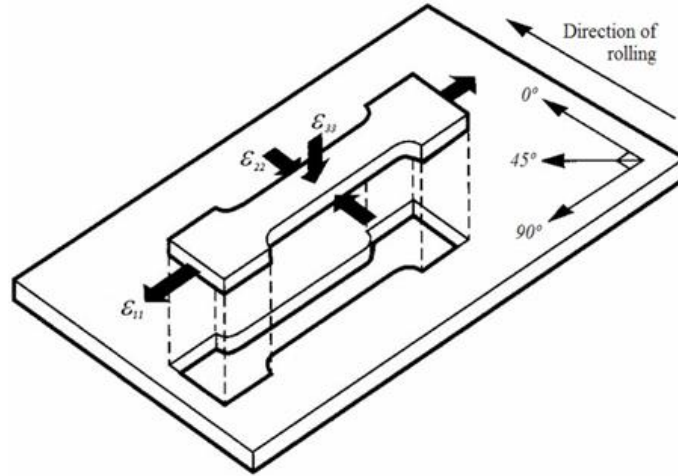
Figure 26: Tensile test specimen of rolled sheet showing strain directions (Vincze 2007) (Kudrathon 2010).

Assuming that plastic deformation occurs at constant volume, ε_{33} can be calculated as:

$$\varepsilon_{33} = -(\varepsilon_{11} + \varepsilon_{22}) \tag{15}$$

where:

$$\varepsilon_{11} = \ln\left(\frac{l}{l_o}\right) \tag{16}$$

with l_0 and l being the initial and final length of the sheet specimen respectively.

Taking into account the equations 12 and 15, R can be calculated using the following equation:

$$R = -\frac{\varepsilon_{22}}{\varepsilon_{11} + \varepsilon_{22}} \tag{17}$$

The average value of R or normal anisotropy coefficient ($\bar{R}$) is calculated from three R-values measured at angles (θ) equal to 0° (R_0), 45° (R_{45}) and 90° (R_{90}) with respect to the rolling direction (RD), using the equation:

$$\bar{R} = \frac{R_0 + 2R_{45} + R_{90}}{4} \tag{18}$$

The variation of the Lankford coefficient with the angle on the sheet plane is given by the planar anisotropy coefficient (ΔR):

$$\Delta R = \frac{R_0 - 2R_{45} + R_{90}}{2} \tag{19}$$

An increase of $\bar{R}$ value is an indication that the material deforms more before rupture and, therefore, the formability increases. If the variation of R (ΔR) is high, the final part may present "ears" (Figure 27) which represents wastage of material and a need of additional processing operations.
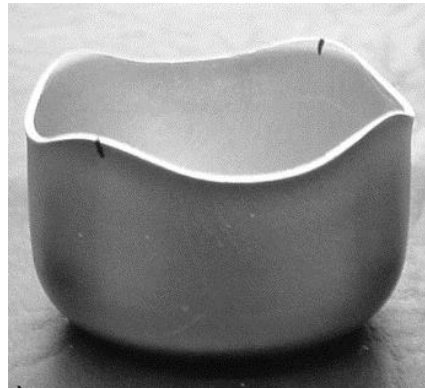
Figure 27: Typical appearance of a deep drawn cup with ears (Engler 2009).

2.3.4.2. Effect of the Amplitude of Strain Path Change

The mechanical behavior of the material depends on the initial texture and the dislocation structure and their respective evolutions during plastic deformation. Usually, the sheet forming

processes involve several sucessive deformation steps. During each strain path, changes can occur on the dislocation structures and crystalographic orientations of the grains that can significantly change the mechanical behaviour of the material during the process.

Depending of the prestrain value and amplitude of the strain path change, the mechanical behavior during reloading can be categorized into three different types, which are shown schematically in Figure 28.
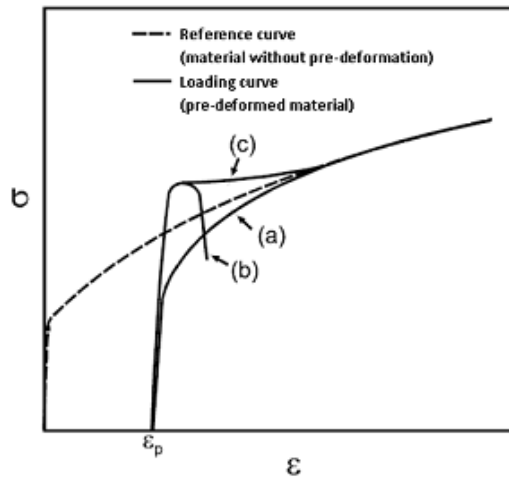
Figure 28: Stress (σ) – strain (ε) curve showing the consequences of reloading after a pre-deformation comparing with the initial monotonic test (Vieira 1994) (Lopes 2001).

From the above figure, curve (a) represents the case where the yield stress during reloading is lower than the yield stress exhibited by the undeformed material, which is the characteristic of a Bauschinger type behavior. In curves (b) and (c), the yield stress during reloading is higher than that of the material without pre-deformation. Curve (b) represents the situation of a premature failure due to softening during the early stage of reloading whereas in curve (c), the material exhibits a similar strain rupture compared with the undeformed material.

The effect of strain path change can be expressed by the cosine of the angle between the two vectors that represent the two successive strain paths defined in the strain space (Schmitt 1994):

$$\alpha = \frac{\varepsilon_p : \varepsilon}{\sqrt{\varepsilon_p : \varepsilon_p}\sqrt{\varepsilon : \varepsilon}} \tag{20}$$

where α is the amplitude of the strain path change and ε_p and ε represent the strain tensors of the prestrain and reloading, respectively. The value of α is related with the change of slip system activity and it varies between -1 (the inversion of strain paths: Bauschinger tests) and 1 (no change of strain path: monotonic tests).

For $\alpha=1$, the slip systems activated before and during the reloading are the same and no change in mechanical behavior is observed. For $\alpha= -1$, the slip systems activated during pre-strain are reactivated in the opposite direction during the reloading and the material presents the typical mechanical behavior of the curve (a) in Figure 28.

When $\alpha=0$, the slip systems that were latent during the prestrain are activated during reloading. A higher reloading stress is required to initiate the movement of dislocations in the new slip systems due to the low prestrain dislocation mobility. However, after the initial stage, dislocation annihilation occurs replacing the prestrain dislocation structure by a structure typical to the second loading and the effect of prestrain on the flow stress decreases. As a result, transient softening occurs (curves (b) and (c) in Figure 28) that can lead to strain localization after the beginning of reloading (curve (b) in Figure 28) . For the same strain path change amplitude value, the decrease of the formability during the reloading is more significant for higher prestrain values.

3. Initial Material and Experimental Procedures

The main objective of this work was to study the effect of the plastic deformation by single point incremental forming on the crystallographic texture, dislocation structure and mechanical properties of aluminum, low carbon steel and dual phase steel sheets.

To characterize the mechanical behavior of the as-received sheets, tensile tests were conducted at angles of 0°, 45° and 90° with respect to the rolling direction. Crystallographic texture characterization was done by electron backscattering diffraction (EBSD) whereas scanning electron microscopy (SEM) and transmission electron microscopy (TEM) were used for the microstructural characterization. The rolled sheets were deformed using the SPIF machine developed at the University of Aveiro (M. Martins 2011) (Torrão 2013) to produce square based pyramidal shapes with 40 mm height and 45° wall angle. Strain and microhardness measurements were performed on the deformed materials to characterize the mechanical behavior. The crystallographic texture and microstructure of the materials after SPIF were characterized by EBSD, SEM and TEM techniques. These analyses were complemented with calculations using a polycrystal plasticity model.

3.1. Initial Materials

The three different materials studied were the aluminum 1050 (AA1050) produced by ALCOA (USA), low carbon (LC) steel from Sollac (France) and dual phase steel (DP780) from POSCO (South Korea). The materials were received as sheets with around 1mm thickness and their respective chemical compositions are presented in the following tables.

Table 3: Chemical composition of aluminum AA1050.

Element	Al	Si	Fe	Cu	Mn	Mg	Cr	Ni	Zn	Ti	Ga	V
Mass ,%	Bal.	0.089	0.280	0.002	0.001	0.001	0.001	0.003	0.005	0.011	0.016	0.007

Table 4: Chemical composition of LC steel.

Element	Fe	C	Mn	P	S	N	Al	Si
Mass, %	Bal.	0.046	0.261	0.012	0.01	0.004	0.043	0.04

Table 5: Chemical composition of DP780 steel.

Element	Fe	C	Si	Mn	P	S	Al_{tot}	Cr+Mo	Nb+Ti	V	B
Mass, %	Bal.	0.080	0.30	1.56	0.020	0.004	0.020	0.74	0.015	0.02	0.001

3.2. Uniaxial Tensile Test

From the initial sheets, rectangular strips were cut at the angle (θ) equal to 0°, 45° and 90° with respect to rolling direction of the sheets (RD). A CNC machine was used to produce the ASTM standard tensile specimens measuring 150 mm x 24mm, as shown in Figure 29. To confirm the reproducibility of the results, at least three samples were tested for each angle and each material.

The tensile properties of the as-received sheets were determined by performing uniaxial tensile tests using a universal testing machine, Shimadzu Autograph with a maximum load capacity of 100kN. A non-contact video extensometer MFA-25 was used to determine the instantaneous length and width of the samples during the experiments. All the tests were conducted at room temperature and at a strain rate of 10^{-3} s^{-1}.
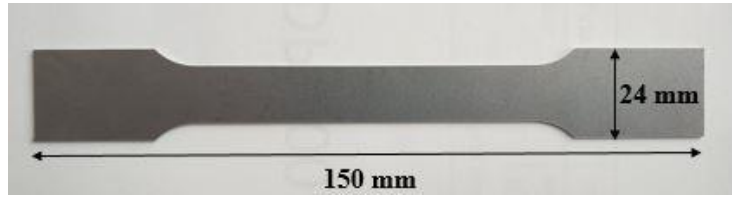
Figure 29: Uniaxial tensile specimens used to perform tensile tests for all the materials.

From the measured applied force (F) and length (l) of the sample during the tests, were calculated the true stress (σ) and true strain (ε) for all the samples using the following equations:

$$\varepsilon = \ln\left(\frac{l}{l_0}\right) \tag{21}$$

$$\sigma = \frac{F}{A_0}\exp(\varepsilon) \tag{22}$$

where, ε is the true strain along the tensile axis, l_0 and A_0 are the initial length and cross section area of the sample, respectively.

From the measurement of the width of the initial samples (w_0) and during the tensile tests (w), the anisotropy coefficients (R) were calculated using the equation:

$$R = \frac{\ln\left(\frac{w}{w_0}\right)}{-\left[\ln\left(\frac{l}{l_0}\right)+\ln\left(\frac{w}{w_0}\right)\right]} \tag{23}$$

3.3. Crystallographic Texture Analysis

The crystallographic texture analysis of the samples were performed using the EBSD technique. A Bruker CrystAlign QC 400 EBSD system attached to a Hitachi SU-70 SEM was employed to map the crystallographic orientations of the grains. The samples were subjected to mechanical polishing using 180, 400 and 1000 grit SiC papers and then to electropolishing using a Struers Lectropol-5 system and a Stuers A2 electrolyte solution. The other relevant parameters used in this process are below in the next table.

Table 6: Parameters used for electropolishing of samples before EBSD analysis

Material	Voltage (V)	Flow Rate	Time (s)
Aluminum	15	9	15
LC Steel	40	14	12
DP780	35	14	20

The EBSD analysis were performed using a 25 keV electron beam and a sample tilt angle of 70º. For each area analyzed, the diffraction patterns of 800x600 points were collected and processed by the system. This results were used to obtain both the crystallographic orientation maps and the data that were used as an input for the crystal plasticity calculations using the viscoplastic self-consistent (VPSC) code developed by Lebensohn and Tomé (R. A. Lebensohn 1993) (R. A. Lebensohn 1994) to evaluate the effect of crystallographic texture on the mechanical behavior of the materials.

3.4. Transmission Electron Microscopy

To study the evolution of dislocation structure during the SPIF process, TEM observations were made in both the as-received and deformed samples using a Hitachi H-9000 microscope. The samples were mechanically polished until less than 100µm thickness using 120, 180, 400 and 1000 grit SiC papers. Discs with 3mm diameter were cut and further thinning was done by Struers Tenupol-3 twin-jet electropolishing system until perforation. The composition of the electrolyte and the voltage applied for the samples are presented in next table.

Table 7: Composition of the electrolyte and voltage applied during the electrolytic thinning process for TEM observations

Material	Electrolyte	Voltage (V)
AA1050	25% (vol.) nitric acid (60% conc.) and 75 % (vol.) methanol	10
LC and DP780 steels	5% (vol.) perchloric acid (60% conc.) and 95% (vol.) ethylene glycol	35

3.5. Single Point Incremental Forming (SPIF)

From the as-received sheets specimens measuring 15 x 15 cm were cut and subjected to SPIF to produce square based pyramidal shapes of 40 mm height and 45° wall angle (Figure 30) using a dedicated system developed at the University of Aveiro (Figure 31). Prior to deformation, the samples were grid marked on the surface in order to perform strain measurements. During the SPIF process, the metallic sheet was restrained by a blank holder and deformed in an area of 9x9 cm with a hemispherical tool tip with 10 mm diameter, using a step down size of 0.5 and a feed rate of 3000 mm/min and unidirectional movement. To reduce friction between the sheet surface and the tool tip, Finarol Total oil was used as lubricant. The deformed samples were then cut using water-jet cutting and smaller samples were further cut from the obtained pieces for additional characterization studies.
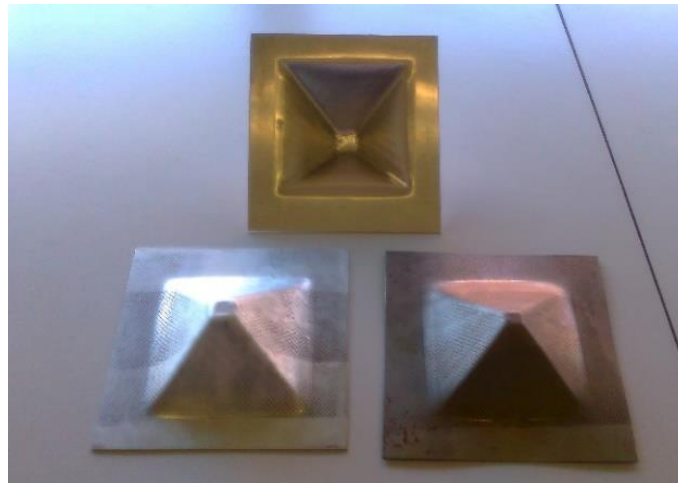
Figure 30: Samples after SPIF.

Figure 31: SPIF machine used in this work.

3.6. Strain Measurements

The strain measurements were carried out on the samples by measuring the diameters of the circular grid previously marked on the external surface (surface that is not in contact with the deformation tool during the SPIF process) of the pieces. The measurements were done using an optical microscope with image acquisition and an average of at least three measurements were taken for consistency. The true strains were calculated using the following equations:

$$\varepsilon_{11} = \ln\left(\frac{d_1}{d_1^0}\right) \qquad (24)$$

$$\varepsilon_{22} = \ln\left(\frac{d_2}{d_2^0}\right) \qquad (25)$$

where ε_{11} and ε_{22} represent the major and minor true strains respectively. d_1 is the diameter of the circle measured perpendicular to the movement of the tool and d_2 is the diameter measured parallel to the direction of the tool movement. d_1^o and d_2^o are the corresponding initial values of d_1 and d_2 measured in as-received sample.

Thickness measurements were also made on all the SPIF pieces by using optical microscopy and an average of three values were used for each point.

3.7. Microhardness Measurements

Microhardness tests were performed using a Shimadzu Vickers microhardness tester type M with a load of 0.2 kgf for aluminum and 0.3 kgf for LC and DP steel and a dwell time of 30 s. These measurements were performed on the external surface of the pieces and an average of at least three readings were taken for all samples at different distances from the center. The indentations were measured using an optical microscope connected to a previously calibrated acquisition image system. The hardness was calculated using the following equation:

$$HV = 1.8544 \times \left(\frac{F}{d^2}\right) \tag{26}$$

where HV represents the Vickers hardness value (kgf/mm^2), F is the applied load (kgf) and d is the average length of the diagonal of the indentation (mm).

4. Results and Discussion

4.1. Initial Material

4.1.1. Aluminum

4.1.1.1. Mechanical Behavior Characterization

Figure 32 represents the true stress-true strain curves obtained from the uniaxial tensile tests in the as-received aluminum sheet at different loading angles. The various parameters extracted from these tests are shown in Table 8.
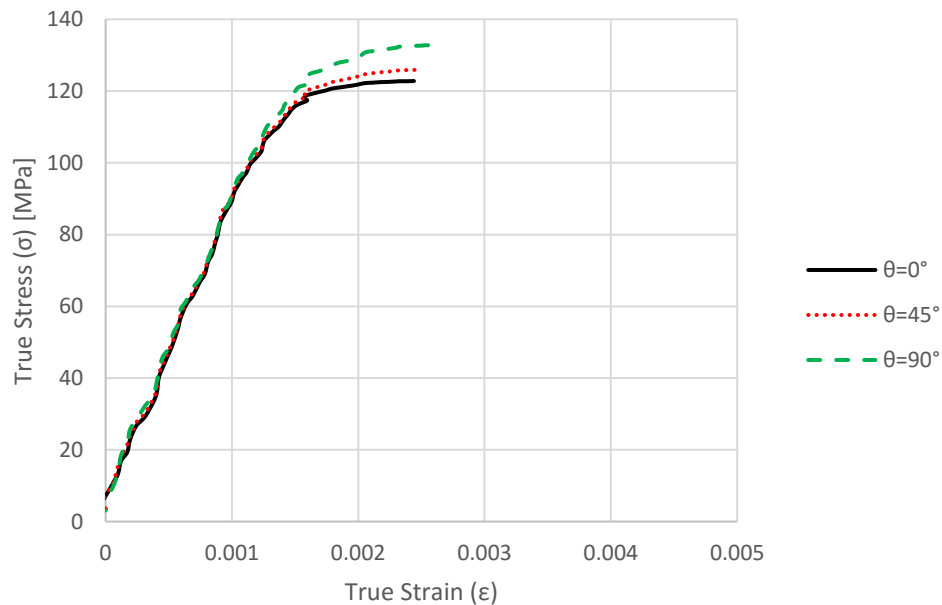
Figure 32: True stress vs true strain for as-received AA1050 at 0°, 45° and 90° from RD.

It is possible to see in the above figure that all the curves are almost identical in behavior but, the yield stress and the uniform strain for the sample tested at an angle of 90° are higher than that of 0° and 45°. Moreover, the comparison of the yield stress and uniform deformation values obtained

in the tests with the typical values of recrystallized AA1050 (around 50 MPa and 30%) (Lopes 2001) (Fábio 2008) allow to conclude that the aluminum sheet was supplied in a highly hardened state. The R-values measured at the different loading angles showed similar values.

Table 8: Yield stress (σ_o), maximum stress (σ_{max}), uniform strain (ε_u), R-value, $\overline{R}$ and ΔR extracted from the tensile tests performed along the different directions of as-received AA1050 sheet.

Material	Θ (°)	Yield Stress, σ_o [MPa]	Max. Stress, σ_{max} [MPa]	Uniform Strain, ε_u (%)	R-value	Normal Anisotropy($\overline{R}$)	Planar Anisotropy,(ΔR)
AA1050	0°	122	123	0.24	2.69	2.74	-0.035
	45°	124	126	0.25	2.76		
	90°	129	133	0.27	2.76		

4.1.1.2 Crystallographic Texture Characterization

The {1 0 0} and {1 1 1} pole figures and $\varphi_2 = 0°$, 45° and 65° sections of Euler space measured in the as-received aluminum are presented in Figure 33 and Figure 34, respectively.
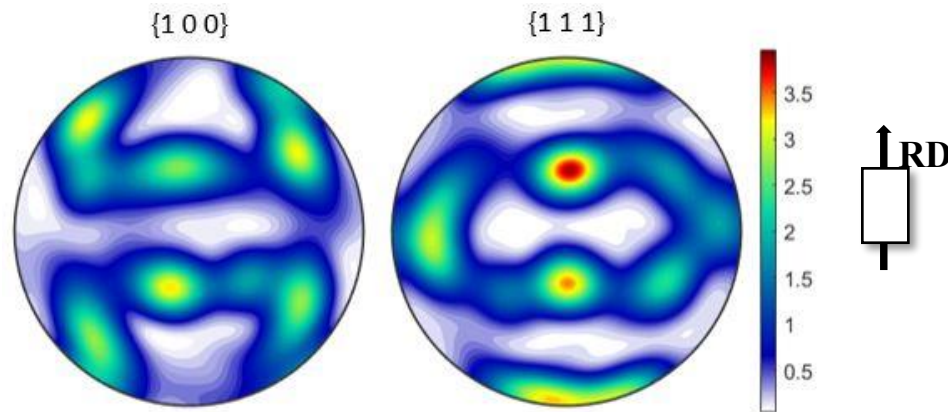
Figure 33: Experimental {1 0 0} and {1 1 1} pole figures of as-received AA1050 sheet.
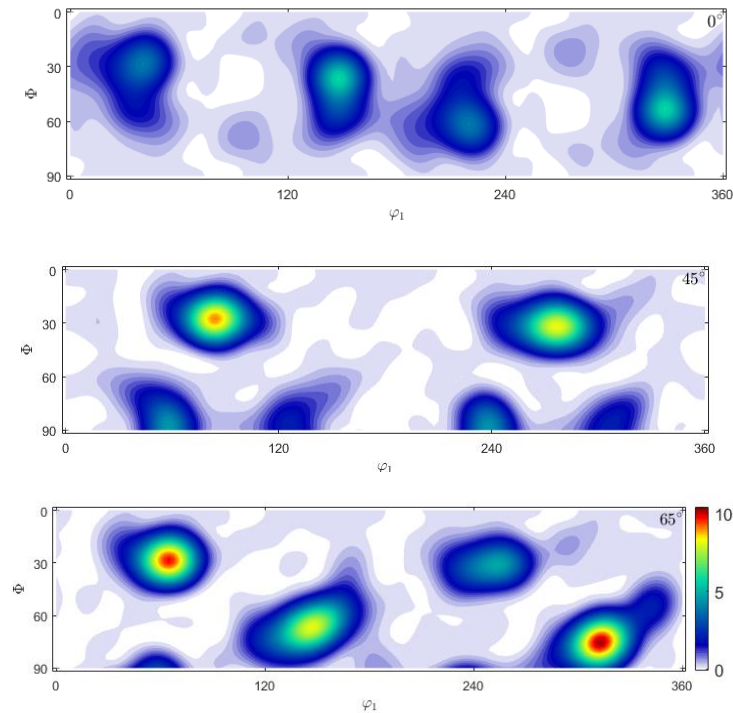
Figure 34: Crystallographic texture of as-received aluminum at $\varphi_2 = 0°$, 45° and 65° sections of Euler space.

From the analysis of these images, it is possible to conclude that the texture exhibited by the as-received aluminum is typical of rolled aluminum. Indeed the comparison of Figure 34 and Figure 24 (b) shows the reinforcements of Copper (Cu) {1 1 2}<1 1 1>, Brass (Bs) {1 1 0}<1 1 2> and S {1 2 3}<6 3 4> (Fábio 2008).

To investigate the contribution of texture on the properties of the as-received material, VPSC model was used to predict, from the experimental crystallographic textures, the evolution of the average Taylor factor (<M>) with the plastic strain along the tensile direction (ε) (Figure 35). Figure 36 shows the variation of the initial average Taylor factor, <M> with the loading angle (θ). For comparison, in the same figure is presented the values of yield stress (σ_o) extracted from the experimental σ-ε curves.
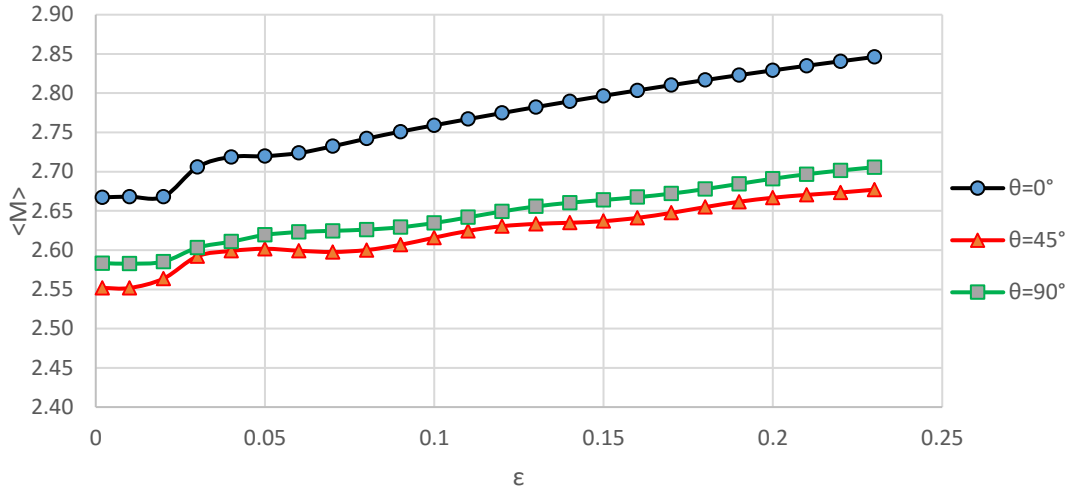
Figure 35: Average Taylor factor (<M>) – strain (ε) values predicted by the VPSC model for as-received AA1050 sheet deformed along different directions (θ).
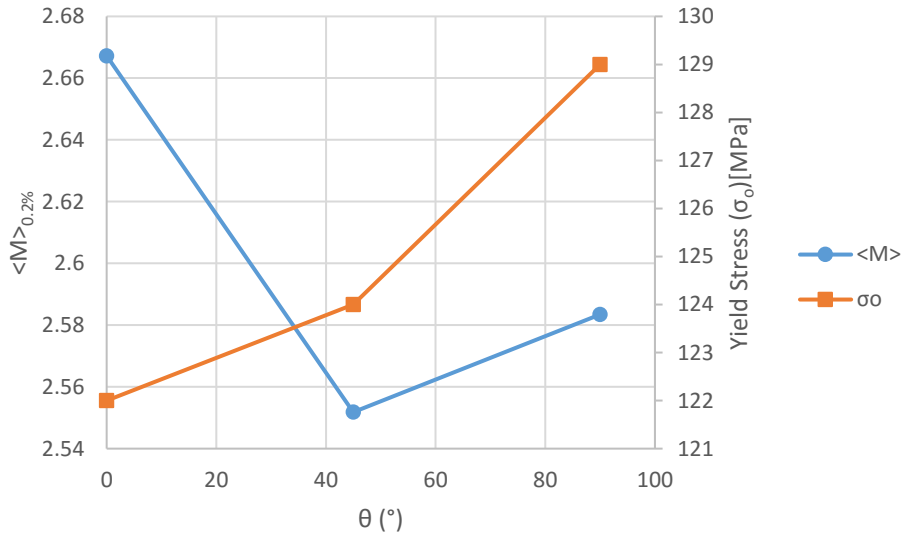
Figure 36: Evolution of the initial <M> predicted by the VPSC model and the experimental yield stress (σ_o) value with the tensile test angle (θ) for the as-received AA1050 sheet.

The VPSC model was also used to predict the values of the anisotropic coefficients of the as-received material. The obtained results are presented and compared with the experimental R values

for the different test angles in Figure 37. The respective normal and planar anisotropic values are shown in Table 9.
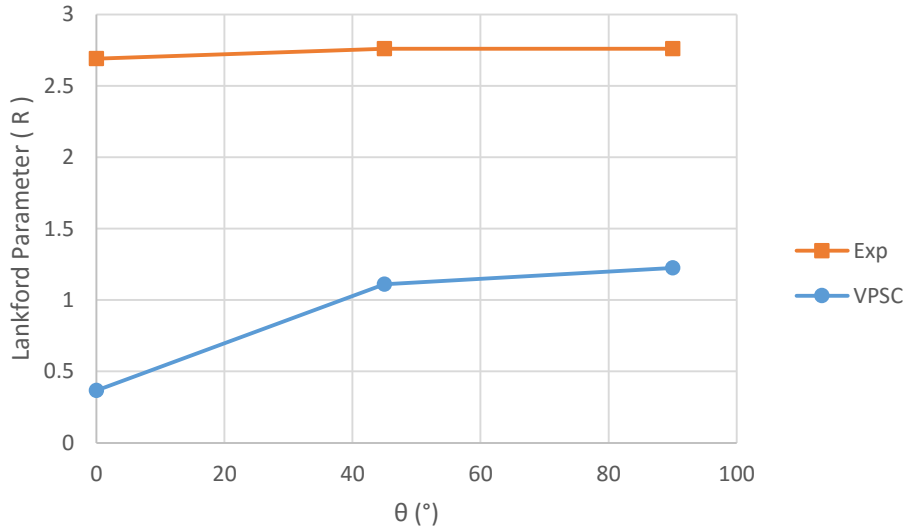
Figure 37: Experimental (Exp) and predicted (VPSC) R values for different loading angles (θ) for as-received AA1050 sheet.

Table 9: Experimental and predicted normal ($\bar{R}$) and planar (ΔR) anisotropy values for as received aluminum.

	Experimental	VPSC
Normal Anisotropy($\bar{R}$)	2.74	0.96
Planar Anisotropy(ΔR)	-0.035	-0.32

From Figure 36, it is possible to verify that the evolution with the loading angle, of the experimental values of yield stress and the predicted <M> values are very different. Namely, the yield values show an increase with θ and while the VPSC model predict a decrease of the <M> value (and therefore of the yield stress) for 45º and a less marked increase for 90º. Also, the comparison of the experimental and predicted anisotropy values (Figure 37 and Table 9) show significant differences. These discrepancies between the experimental and predicted values

strongly suggest that both the stress and strain anisotropy of the AA1050 cannot be attributed to the initial crystallographic texture of the material but has a microstructural origin.

Assuming that the hardened state of the as-received AA1050 sheet is a result of the rolling deformation during its production, it was calculated from equation 20 the evolution of the α parameter with the reloading angle for a sequence of rolling-tensile tests. The obtained results are presented in Figure 38 and allows to see that, for the tensile test performed at 90° from a prestrain rolling direction α is zero, which represents a situation where the slip systems that were latent during the prestrain are activated during reloading. This condition usually corresponds to a higher reloading yield stress, as experimentally observed in this work for AA1050 sheet. For $\theta=0$°, the α value is maximum and close from 1, which correspond to a situation where the slip systems activated before and during the reloading are the same and therefore, the yield stress presents a lower value. For $\theta=45$°, the α value is 0.4 which correspond to a yield stress between the values presented by the other two tested directions, as was observed during the tensile tests of AA1050.
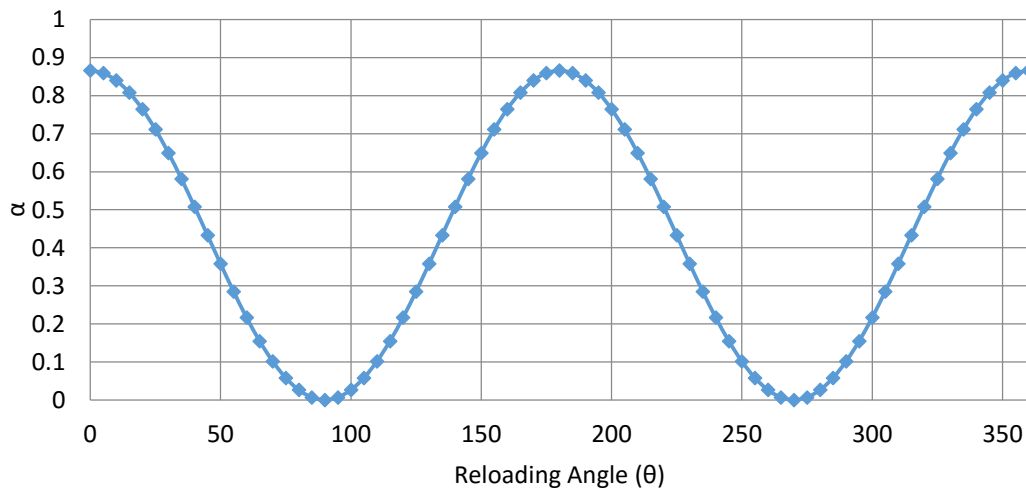
Figure 38: Evolution of α parameter with the reloading angle (θ) for a sequence of rolling-tensile tests.

4.1.1.3. Microstructure Characterization

The TEM observations performed on the as-received material (Figure 39) revealed a microstructure defined by sub-grains with around 2µm size and low concentration of dislocations inside. This microstructure is frequently observed in low alloyed and high stacking fault energy metals, such the AA1050, deformed up to large strain values. Indeed, several studies showed that both characteristics contributes for the high mobility of dislocations in these materials and facilitates the development of dislocation cells during the first stage of plastic deformation that with the increase of strain, evolve to sub-grains. Therefore, the observed microstructure is another experimental result that supports the above conclusion that the AA1050 sheet was supplied in highly hardened state.

In Figure 40 is presented the orientation maps obtained by EBSD analysis where it is possible to identify the presence of relatively large regions with similar orientation along the rolling direction and, at smaller scale, sub-grains with different crystallographic orientations. It is worth to say that the crystallographic misorientations between different sub-grains, characteristic of this type of microstructure, was also observed by TEM electron diffraction.
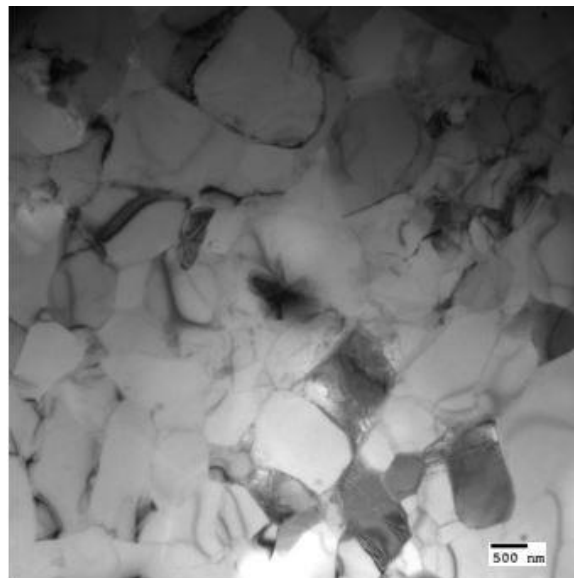
Figure 39: TEM image of as-received aluminum.
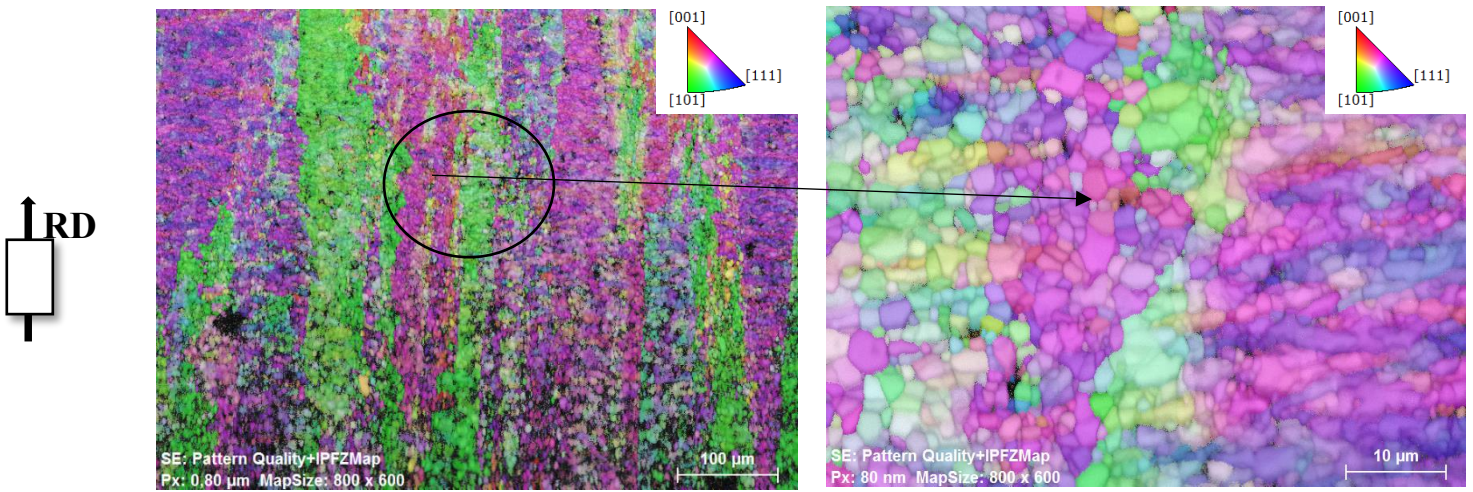
Figure 40: Orientation maps obtained by EBSD on as-received aluminum.

4.1.2. Low Carbon Steel

4.1.2.1. Mechanical Behavior Characterization

The true stress-true strain curves obtained from the uniaxial tensile tests performed on the as-received LC steel sheet at different loading angles (θ) are presented in Figure 41.
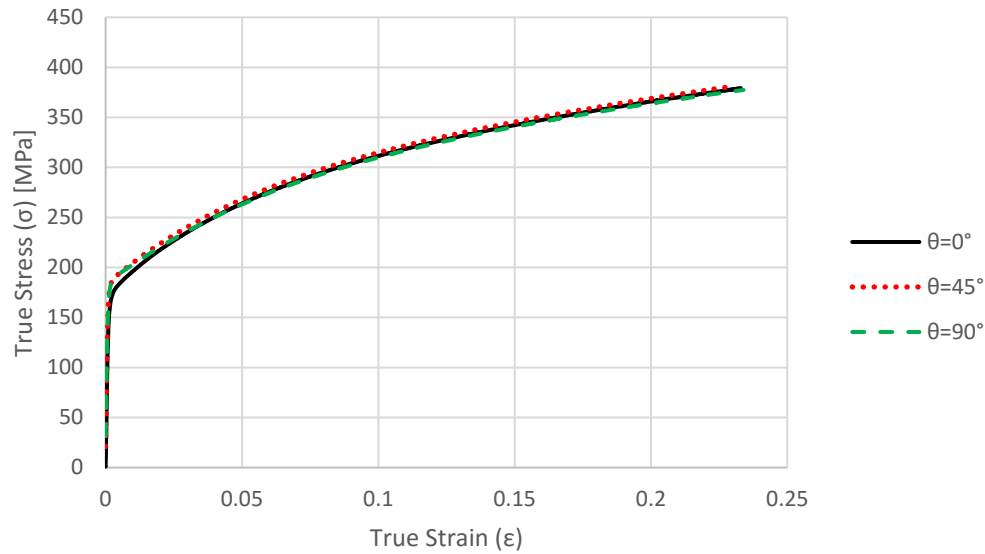
Figure 41: True stress vs true strain for as-received LC steel at 0°, 45° and 90° from RD.

These results show a similar tensile behavior for all the three test angles. Indeed, except the lower flow stress at the beginning of the tensile tests for the loading at 0°, the three curves almost superpose. This similarity is also expressed by the identical values of yield stress, maximum stress and uniform strain calculated from the curves and presented in Table 10. However, different R values were measured along the three directions. More specifically, the maximum R value occurs for a loading angle of 90° and similar R-values are shown for the samples loaded at 0° and 45°. These relatively high R values show that the plastic deformation of the LC steel during the tensile tests is anisotropic and the strain along the width (ε_{22}) is higher than along its thickness (ε_{33}), which corresponds to a relatively high capability of the LC steel sheet to deform before failing due to excessive thickness reduction.

Table 10: Yield stress (σ_o), maximum stress (σ_max), uniform strain (ε_u), R-value, $\overline{R}$ and ΔR of the extracted from the tensile tests performed along the different directions of as-received LC steel sheet.

Material	Θ (°)	Yield Stress, σ_o [MPa]	Max. Stress, σ_max [MPa]	Uniform Strain, ε_u (%)	R-value	Normal Anisotropy($\overline{R}$)	Planar Anisotropy,(ΔR)
LC Steel	0°	167	380	23.27	1.72	1.85	0.30
	45°	184	381	23.06	1.70		
	90°	184	377	23.40	2.27		

4.1.2.2. Crystallographic Texture Characterization

Figure 42 and Figure 43 show the {1 0 0} and {1 1 0} pole figures and $\varphi_2 = 0°$, 45° and 65° sections of Euler space, respectively, for the as-received LC steel sheet.
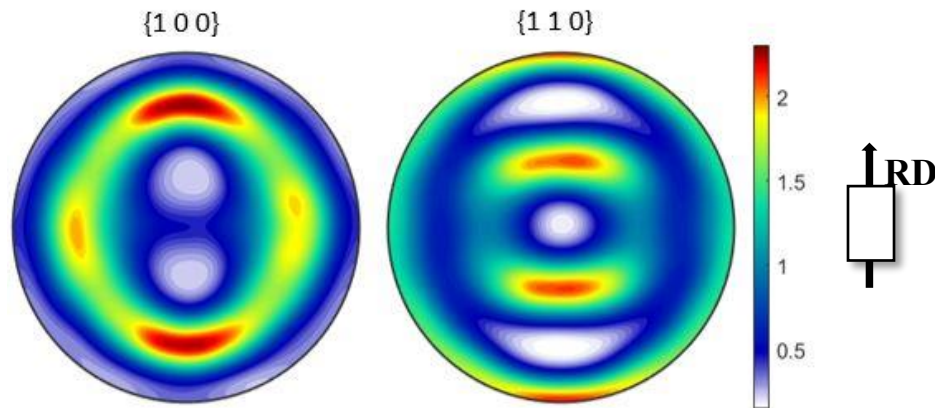
Figure 42: Experimental {1 0 0} and {1 1 0} pole figures of as-received LC steel sheet.
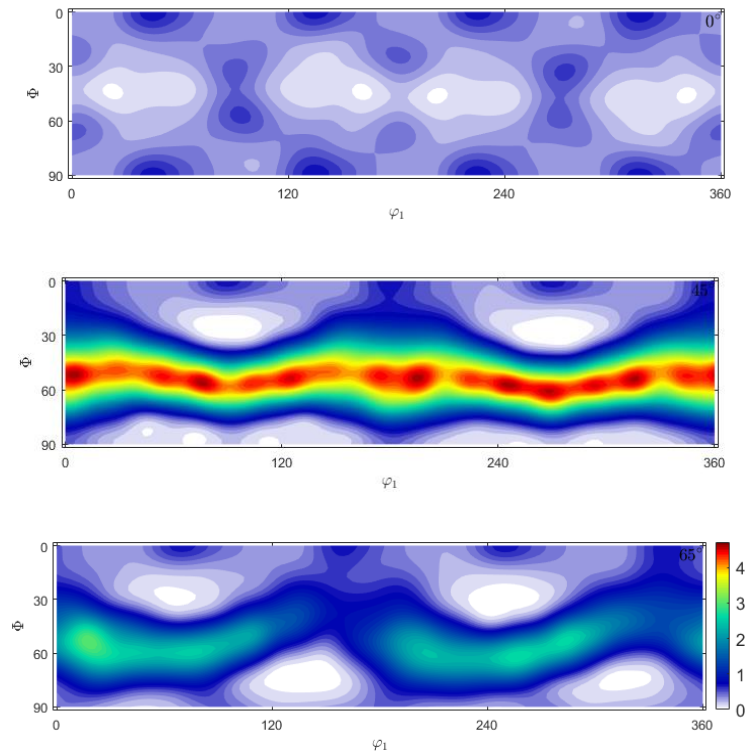
Figure 43: Crystallographic texture of as-received low carbon steel at $\varphi_2 = 0°$, $45°$ and $65°$ sections of Euler space.

The obtained pole figures show a strong γ-fiber ({1 1 1}<u v w>) texture with reinforcement of {1 1 1}<1 1 0> component (that can be confirmed by comparing the Euler section at $\varphi_2=45°$ in Figure 43 with Figure 25), that is typical in rolled steel (Suwas 2014).

Figure 44 shows the evolution of average Taylor factor, <M> calculated from the initial textures for different loading angles (θ) with the tensile plastic strain. These results show that the initial <M> values for $\theta=0°$ is slightly lower for $\theta=45°$ and $90°$, which are almost coincident for all the analyzed range of strain values. However, for higher strains these differences are almost canceled and the three curves almost are superimposed. These evolutions of <M> with the strain are very similar to the evolution of the flow stress experimentally measured during the tensile tests along the three directions. Similar conclusions can also be taken from Figure 45, where are compared the values predicted for <M> and the experimental yield stress. In this last figure, both <M> and σ_o values show a minimum for $\theta=0°$ and a significant increase for $\theta=45°$, after which, are almost

constant. This good agreement between the value of <M> predicted by the VPSC model and the experimental values of stress, strongly suggest that the stress anisotropy observed for the LC steel sheet during the initial stage of the tensile tests has a crystallographic texture origin.
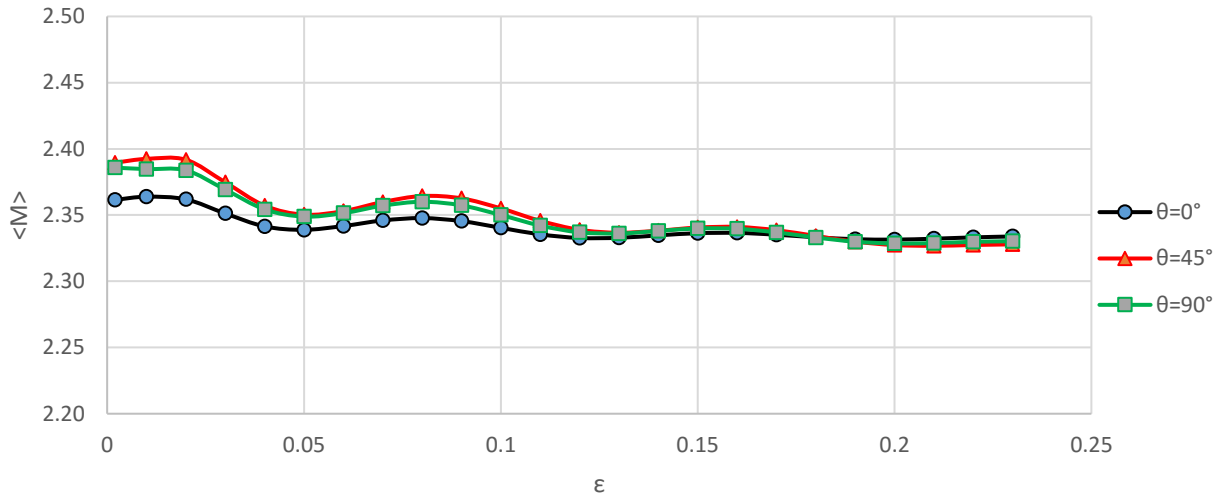
Figure 44: Average Taylor factor (<M>) – strain (ε) values predicted by the VPSC model for as-received LC steel sheet deformed along different directions (θ).
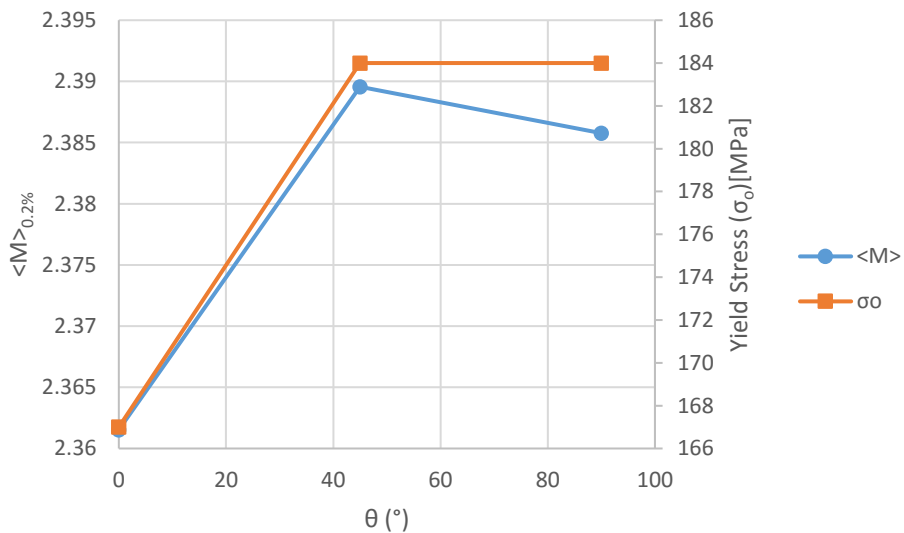
Figure 45: Evolution of the initial <M> predicted by the VPSC model and the experimental yield stress (σ_o) value with the tensile test angle (θ) for the as-received LC steel sheet.

Similar conclusion about the influence of the initial crystallographic texture on the strain anisotropy of the LC steel sheet can be drawn from the comparison of the experimental and predicted R, $\bar{R}$ and ΔR values (Figure 46 and Table 11). From these analysis it is possible to conclude that the VPSC model could predict with a high degree of success both the stress and strain anisotropy presented by the LC steel, allowing to attribute the observed differences observed during the tensile tests in the flow stress and R values to the initial crystallographic texture of the material.
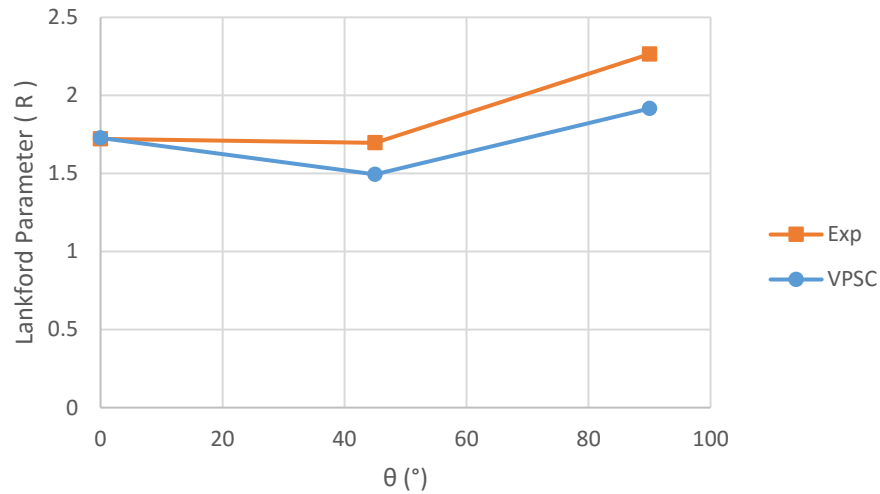
Figure 46: Experimental (Exp) and predicted (VPSC) R values for different loading angles (θ) for as-received LC steel sheet.

Table 11: Experimental and VPSC predicted normal ($\bar{R}$) and planar (ΔR) anisotropy values for as-received low-carbon steel.

	Experimental	VPSC
Normal Anisotropy($\bar{R}$)	1.85	1.66
Planar Anisotropy(ΔR)	0.30	0.33

4.1.2.3. Microstructure Characterization

In Figure 47, is presented the EBSD orientation maps obtained in samples taken from the as-received LC steel sheets. In these images it is possible to clearly identify the equiaxed grain structure with a size of around 30μm. The high uniformity of the color inside each grain is an indication of a low crystallographic misorientation between the different regions of each grain. These microstructural characteristics were also observed by TEM, presented in Figure 48, together with a dislocation structure defined by a low density and uniform distributed dislocations inside the ferrite grains. This dislocation microstructure is typical of recrystallized ferrite, although some dislocations may have been originated by a probable skin pass deformation, usually applied during the production of steel sheets (Grassino 2012).
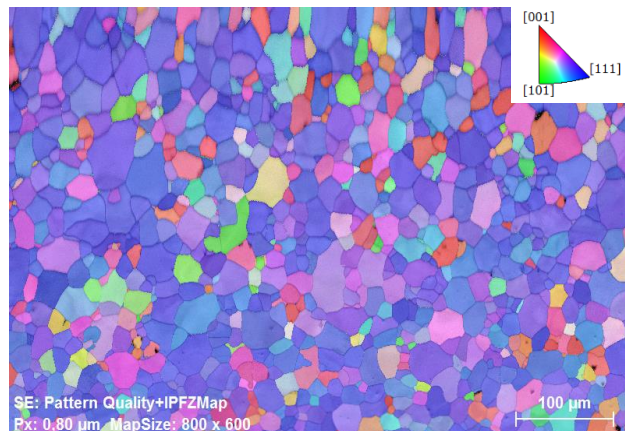
Figure 47: Superimposed EBSD orientation map of initial low carbon steel.
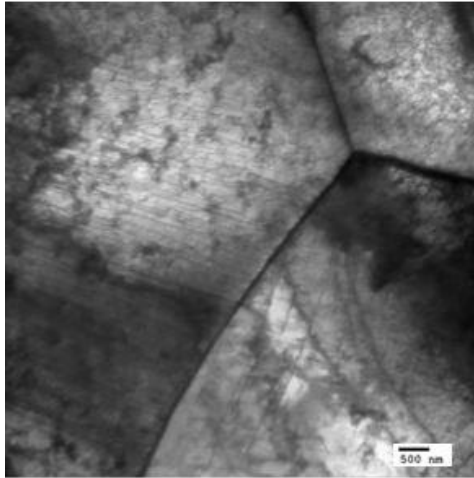
Figure 48: TEM image of LC steel showing the triple point junction.

4.1.3. Dual Phase Steel

4.1.3.1. Mechanical Characterization

The uniaxial true stress-true strain curves for the as-received DP780 steel along the different loading directions are depicted in Figure 49. In Table 12 are presented, the various tensile parameters extracted from these tests.
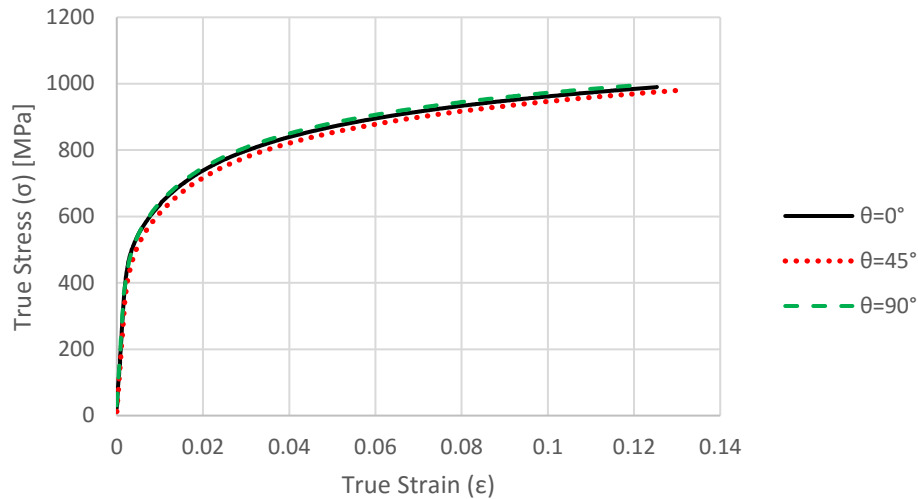
Figure 49: True stress vs true strain for as-received DP780 at 0°, 45° and 90° from RD.

From the tensile curves it is possible to verify that all the three curves show similar behavior with a high initial hardening rate ($d\sigma/d\varepsilon$), which decreases with increasing strain. Moreover, the yield point for DP780 is not very clear, leading to a smooth transition between the elastic and the plastic regions. This differs in the case of LC steel where hardening rate during the initial stage of plastic deformation is significantly lower and the beginning of the plastic deformation is better defined. Another difference between the σ-ε curves obtained in both steels are the higher values of yield and flow stress presented by the DP steel that can be attributed to the presence the martensite (Jiecen 2015). Moreover, the decrease in uniform strain of DP780 compared to LC steel can be explained based on the lower values of R (Table 11) and on the higher strain value accommodated by the ferrite phase in DP steel, for the same macroscopic strain value imposed during the tensile test. Indeed, assuming that the martensite phase remains, at a first approximation, plastically undeformed (Bergström 2010), a relation between the amount of strain experienced by the ferrite grains and the volume fraction of martensite in the material can be formulated:

Before deformation   After deformation

(a)

(b)
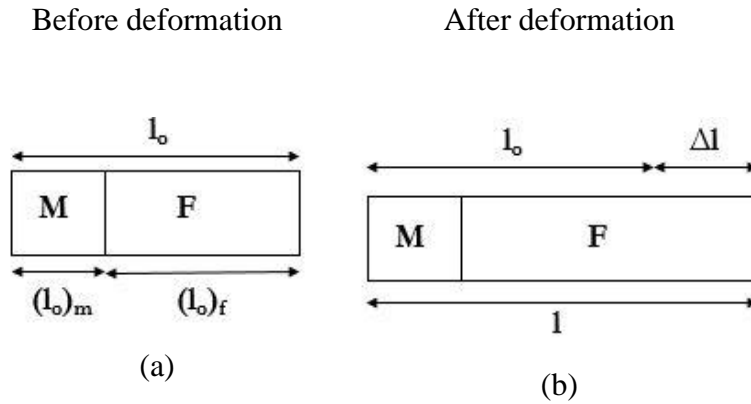
Figure 50: Schematic representation of plastic deformation in DP780; (a) before deformation and (b) after deformation.

From Figure 50, if M and F represent the volume fraction of martensite and ferrite, respectively, l_o the initial length before deformation, $(l_o)_m$ and $(l_o)_f$ the initial length fraction of martensite and ferrite, l the final length after deformation and Δl the change in length during the deformation, the total true strain is given by:

$$\varepsilon = \ln(\frac{\Delta l}{l_o} + 1) \tag{27}$$

Because:

$$(l_o)_f = l_o - (l_o)_m \tag{28}$$

the true strain experienced by the ferrite grains (ε_f) can be calculated by:

$$\varepsilon_f = \ln\left(\frac{\Delta l}{(l_o)_f} + 1\right) = \ln\left(\frac{\Delta l}{l_o - (l_o)_m} + 1\right) \tag{29}$$

This equation shows that the fraction of the macroscopic tensile strain accommodated by the ferrite grains (ε_f) increases with the volume fraction of martensite (increase of $(l_o)_m$) in the material.

Table 12: Yield stress (σ_o), maximum stress (σ_{max}), uniform strain (ε_u), R-value, $\overline{R}$ and ΔR of the extracted from the tensile tests performed along the different directions of as-received DP780 steel sheet.

Material	Test	Yield Stress, σ_o [MPa]	Max. Stress, σ_{max} [MPa]	Uniform Strain, ε_u (%)	R-value	Normal Anisotropy($\overline{R}$)	Planar Anisotropy,(ΔR)
DP780	0°	403	990	12.53	0.84	0.95	-0.12
	45°	363	980	13.02	1.00		
	90°	398	994	11.89	0.93		

Regarding to the strain anisotropy, Table 12 shows that the R values for all the directions are fairly similar and almost equal to 1. As a result, the $\overline{R}$ values is almost unity (indicating a strain distribution in the material almost isotropic) and ΔR is near from zero (indicating a low strain anisotropy in the sheet plane).

4.1.3.2. Crystallographic Texture Characterization

In Figure 51, the {1 0 0} and {1 1 0} pole figures of the as-received DP780 is represented and the corresponding Euler space representation for φ_2= 0°, 45° and 65° sections are shown in Figure 52.
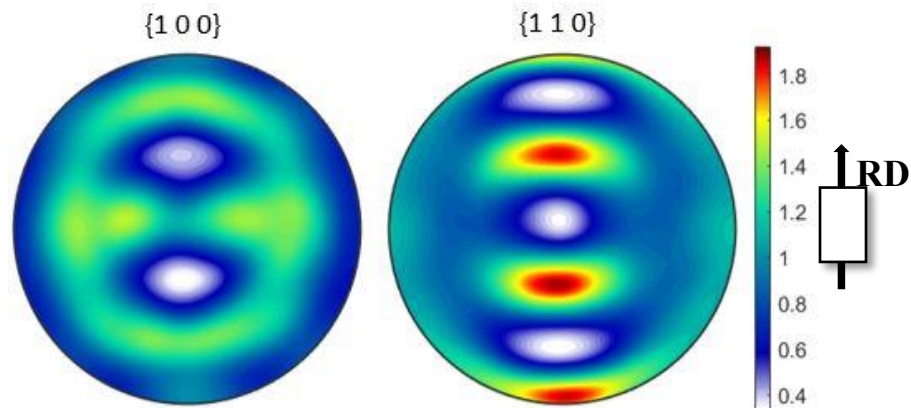
Figure 51: Experimental {1 0 0} and {1 1 0} pole figures of as-received DP780 steel sheet.
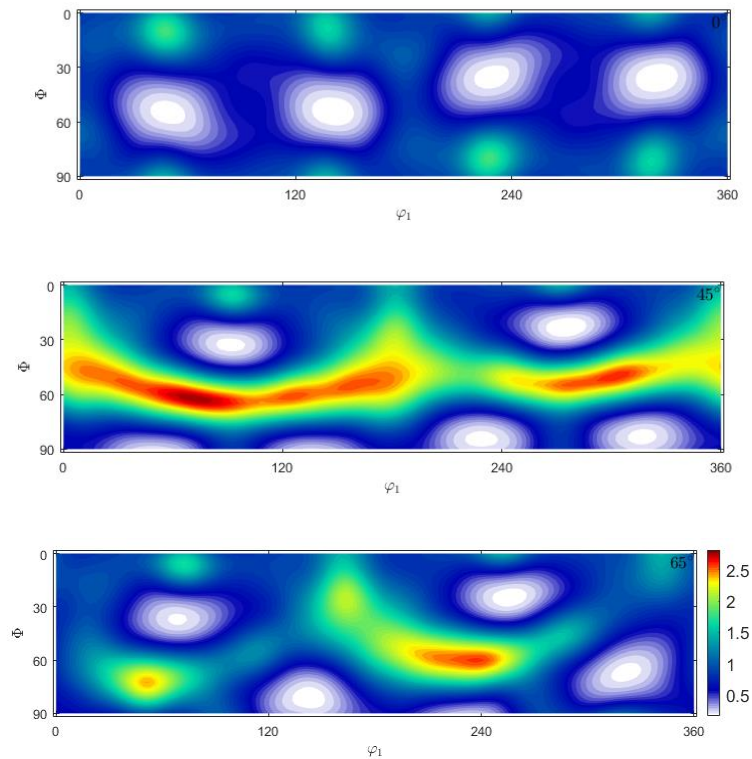
Figure 52: Crystallographic texture of as-received dual phase steel at $\varphi_2 = 0°$, 45° and 65° sections of Euler space.

From both figures it is possible to conclude that the distribution of crystallographic orientations are typical of that of rolled steels, as seen in the case of LC steel (a γ-fiber ({1 1 1}<u v w>) texture with reinforcement of {1 1 1}<1 1 0> component).

To assess the contribution of the ferrite texture on the mechanical behavior, plots of average Taylor factor <M> calculated by VPSC model with the plastic tensile strain were made for the different loading angles (Figure 53 and Figure 54). During these calculations it was assumed that only the ferrite grains would participate in the plastic deformation. From the obtained results it is possible to verify that the <M> evolves similarly with the strain value for all the samples. It is also observed that the evolution of the initial values of <M> with the loading angle agree qualitatively well with the evolution of the yield stress. This is an indication that the difference between the yield stresses in DP780 have, as for LC steel, a crystallographic texture origin.
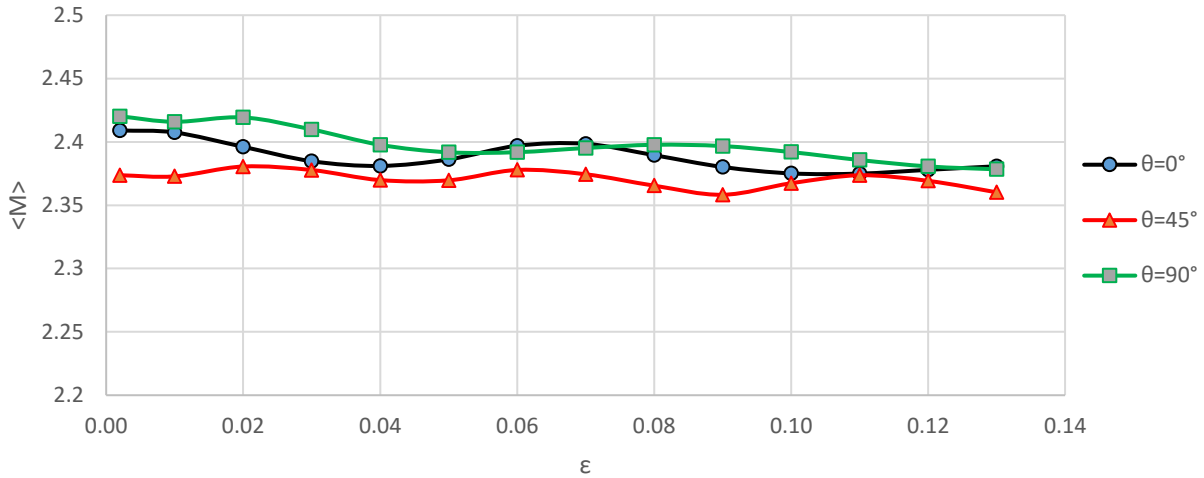
Figure 53: Average Taylor factor (<M>) – strain (ε) values predicted by the VPSC model for as-received DP780 steel sheet deformed along different directions (θ).
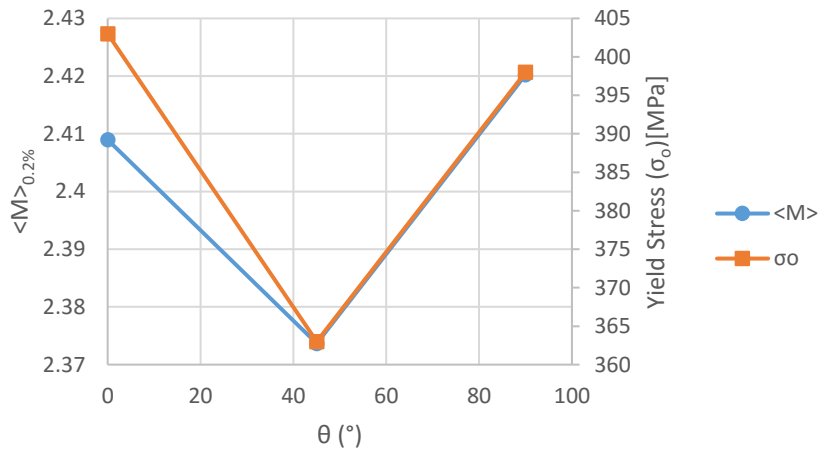
Figure 54: Evolution of the initial <M> predicted by the VPSC model and the experimental yield stress (σo) value with the tensile test angle (θ) for the as-received DP780 steel sheet.

The strain anisotropy coefficients were also computed by the VPSC model for the different test angles. These values are presented in Figure 55 and compared with the R values experimentally measured during the tensile tests. The experimental and predicted normal and planar anisotropy values for the initial material are presented in Table 13. From the analysis of these results it can be concluded that, except the small increase predicted of R for θ=45° to θ=90°, the VPSC model

correctly, qualitatively predicts the strain anisotropy presented by material. This suggests that even the strain anisotropic behavior of the as-received DP780 steel sheet has a crystallographic texture origin.
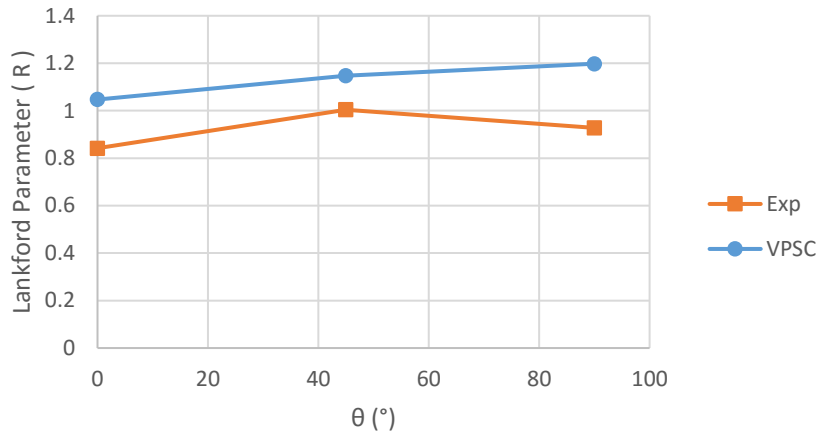
Figure 55: Experimental (Exp) and predicted (VPSC) R values for different loading angles (θ) for as-received DP780 steel sheet.

Table 13: Experimental and VPSC predicted normal ($\bar{R}$) and planar (ΔR) anisotropy values for as-received DP780.

	Experimental	VPSC
Normal Anisotropy($\bar{R}$)	0.95	1.14
Planar Anisotropy(ΔR)	-0.12	-0.03

4.1.3.3. Microstructure Characterization

In Figure 56 is presented a SEM image and an EBSD map obtained from the as-reveived DP780. In Figure 56 (a), the light grey areas correspond to martensite phase areas and the darker grey areas to the ferrite grains. It can be seen from these images that the martensitic islands are distributed homogeneously around the grain, usually in the grain boundary, and the ferrite grains are almost equiaxial. The grain size is about 7μm which is considerably less compared to LC steel.

This lower grain size is an additional factor that explain, together with the presence of the hard martensite phase, the higher flow stress presented by the DP steel than by the LC steel.

(a)   (b)
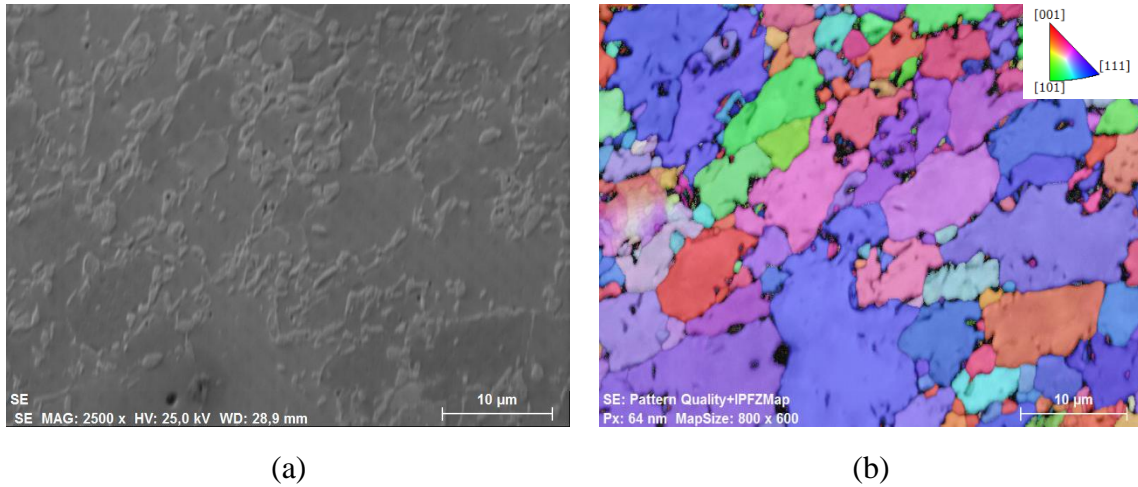
Figure 56: (a) SEM micrograph and (b) EBSD map of the as-received DP780. Due to the small size, the EBSD system cannot identified the crystallographic orientations of the martensite particles, which are represented in image (b) as a black areas.

From the measurement of the relative area fraction corresponding to each phase using a dedicated digital image processing system, the volume fraction of martensite was calculated. From the obtained value (around 35%), the equation 29 and taking into account that the length fraction and volume fraction and of a phase in a multiphase material are equivalent, is was calculated the true strain accommodated by the ferrite phase when a macroscopic tensile strain of 13% (maximum macroscopic uniform strain value exhibited by DP780) is applied to the material. The result of these calculations show that the ferrite grains must deform more about 6.5% then the macroscopic strain imposed to the material during the tensile test (13%) to compensate the inability of the martensitic particles to participate in plastic deformation. Taking into account this correction to the martensite volume, the strain accommodated by the ferrite grains in DP780 and LC steel are more similar (23% and 19%).

4.1.3.4. Transmission Electron Microscopy (TEM)

In Figure 57 is presented TEM images from the observations carried out on the as-received DP780 steel where it is possible to identify the martensite islands as darker regions mostly located in the grain boundaries of the ferrite grains. It is also possible to observe the dislocation structure in the ferrite grains with higher dislocation density than in LC steel. The origin of this increase in the dislocation density is usually attributed to the residual stresses developed during the austenite-martensite phase transformation that occurs during the production of the DP steel (Bergström 2010).
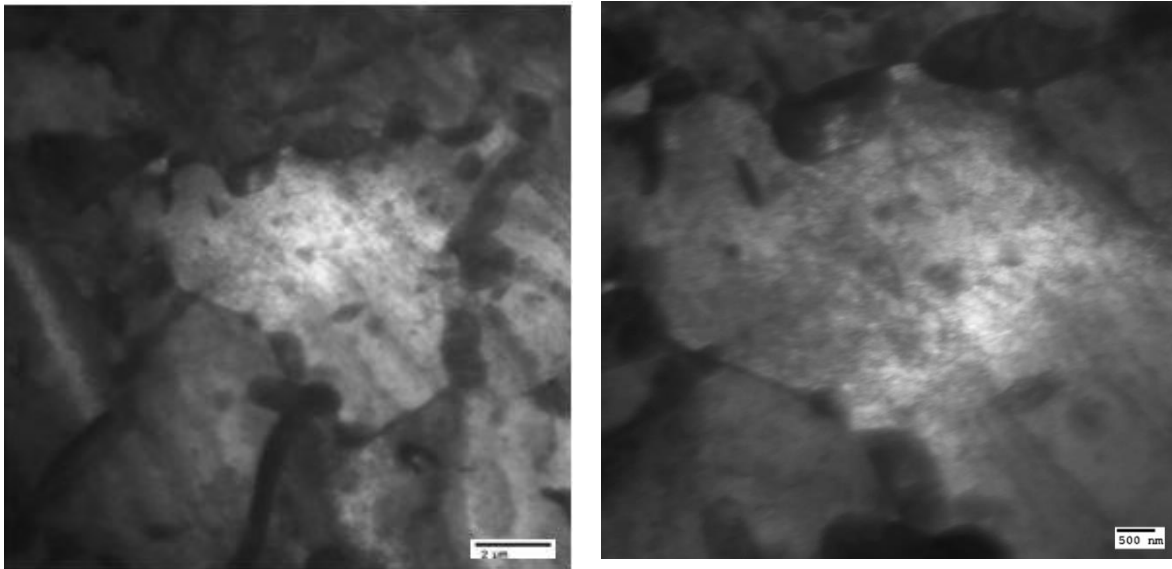
Figure 57: TEM image of as-received DP780.

4.2. Material after SPIF

4.2.1. Aluminum

4.2.1.1. Strain Measurements

The true strains measured perpendicularly (ε_{11}) and along (ε_{22}) the direction of the movement of the deformation tool are plotted with respect to the distance from the center of the AA1050 piece after SPIF in Figure 58.
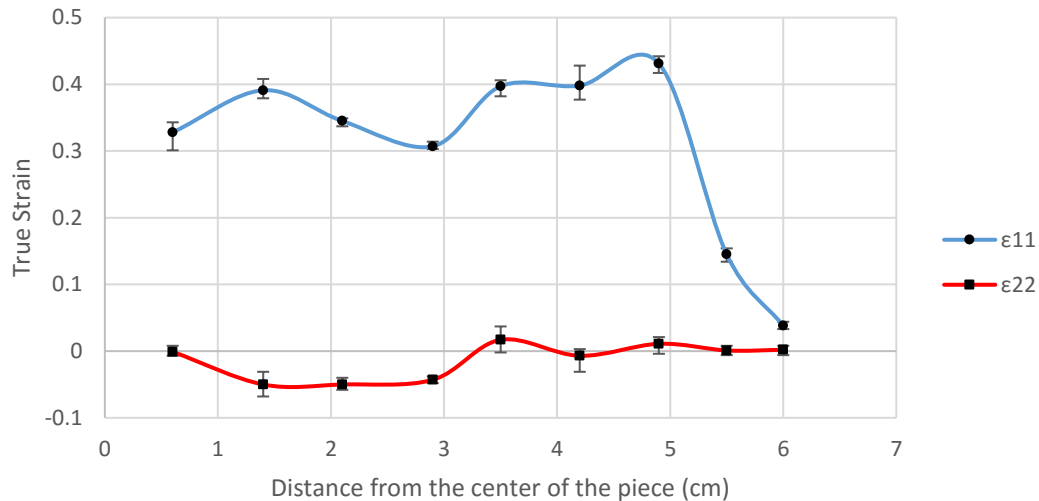
Figure 58: Evolution of the true strains (ε_{11} and ε_{22}) with distance from the center of the AA1050 SPIF piece.

It is seen that the ε_{11} is almost zero further away from the center, where the material was not deformed by the tool, preceding a significant increase before the stabilization in regions more near from the center of the piece. This increase before the stabilization suggests that different deformation modes (such as bending and stretching) are imposed to the material during the initial and later stages of SPIF process.

It should to be highlighted the high values of ε_{11} achieved during the SPIF process without rupture of the material, when compared with the very small uniform deformation showed by the AA1050 sheet during the tensile test.

The more stable and almost null value of ε_{22} is in agreement with the selected shape for the piece that can be obtained from a plane sheet without change in dimension along the direction of the of the deformation tool movement. Another important observation from the previous figure is the more or less regular fluctuation of the strain values that indicates that the plastic deformation is not homogeneous along the piece. This can be attributed to a localized plastic deformation promoted by the tool that can be minimized by increasing the tool diameter and/or decreasing the distance between successive forming steps.

Assuming that the volume of material remains constant during the plastic deformation, is valid the following relationship between the true strain along the thickness (ε_{33}) and ε_{11} and ε_{22} values:

$$\varepsilon_{11} + \varepsilon_{22} + \varepsilon_{33} = 0 \qquad\qquad 30$$

For, $\varepsilon_{22} = 0$,

$$\varepsilon_{33} = -\varepsilon_{11} \qquad\qquad 31$$

From the definition of true strain,

$$\varepsilon_{33} = \ln\left(\frac{t_f}{t_o}\right) \qquad\qquad 32$$

where, t_f and t_o represent the final and initial thickness of the sheet, respectively. Using the sine law (eqn. 1) and t_o=1mm, the previous equations transforms to:

$$\varepsilon_{33} = \ln(\sin(45°)) = -0.347$$

And, therefore:

$$\begin{cases} \varepsilon_{11} = 0.347 \\ \varepsilon_{22} = 0 \\ \varepsilon_{33} = -0.347 \end{cases} \qquad\qquad 33$$

These values are represented as a non-continuous straight lines in next figure, together the experimental values of ε_{11} and ε_{22} and the calculated values of ε_{33} using equation 15. This representation shows a good agreement between the experimental strain values and the values of the previous equation, showing that the sin law (equation 1) can be used to predict the approximate thickness of the AA1050 piece in regions away from the clamped zone.
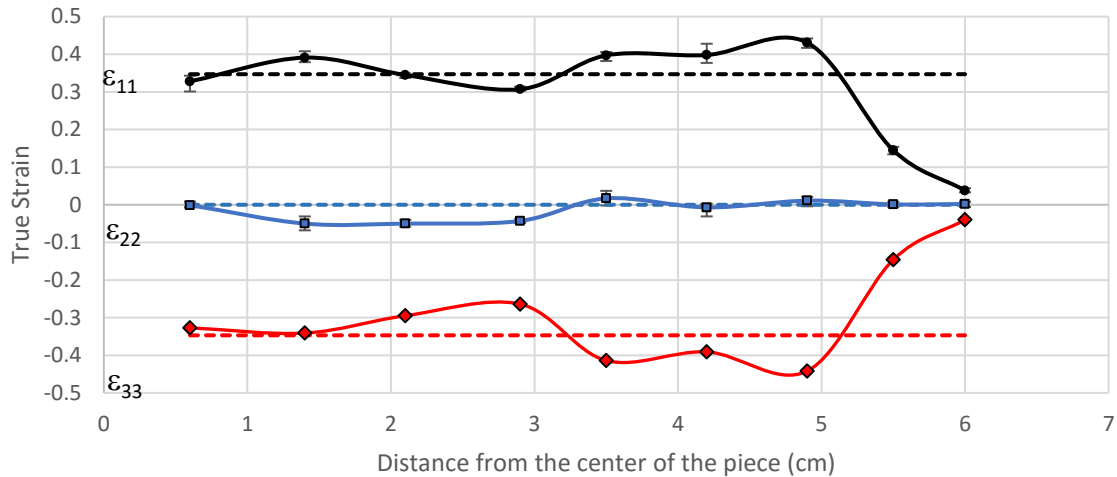
Figure 59: Evolution of the experimental values of ε_{11} and ε_{22} (continuous black and blue lines, respectively) and ε_{33} calculated (continuous red line) from equation 15, with the distance from the center for the AA1050 piece. The non-continuous lines represent the strain values calculated from equation 33.

The comparison of the experimental values of thickness and the values calculated using the experimental ε_{11} and ε_{22} and eqn. 15 and 32 (Figure 60) show a good quantitative agreement. It is also seen that the measured thickness outside from the area deformed by the tool is less than 1mm (thickness of the as-received sheet). This reduction can be attributed to the compressive forces exerted by the clamping system during the SPIF process. Moreover, the curve also confirms the fluctuations observed in the strain measurements of Figure 58.
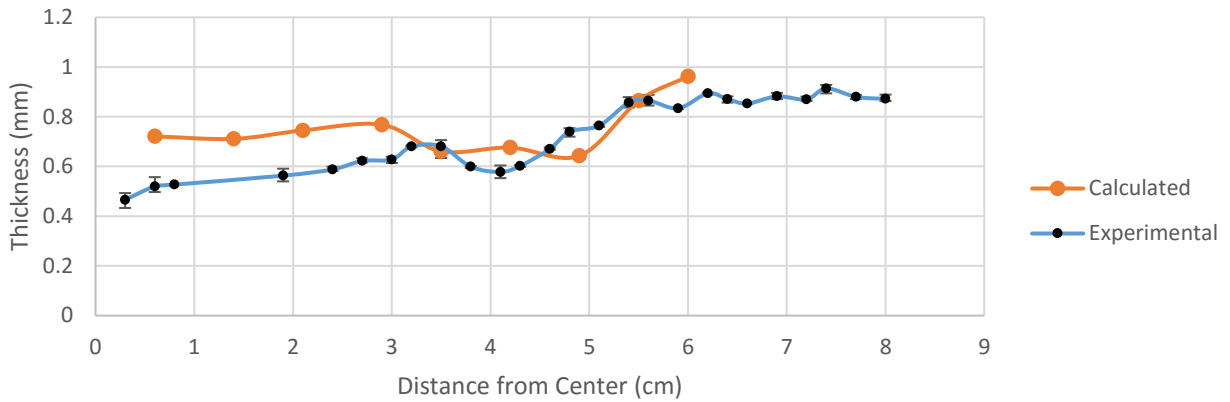
Figure 60: A comparison between the theoretical and experimental thickness of the deformed aluminum sheet.

4.2.1.2. Microhardness Measurements

Microhardness measurements performed on the AA1050 after SPIF process are plotted as a function of the distance from the center of the deformed piece in Figure 61.
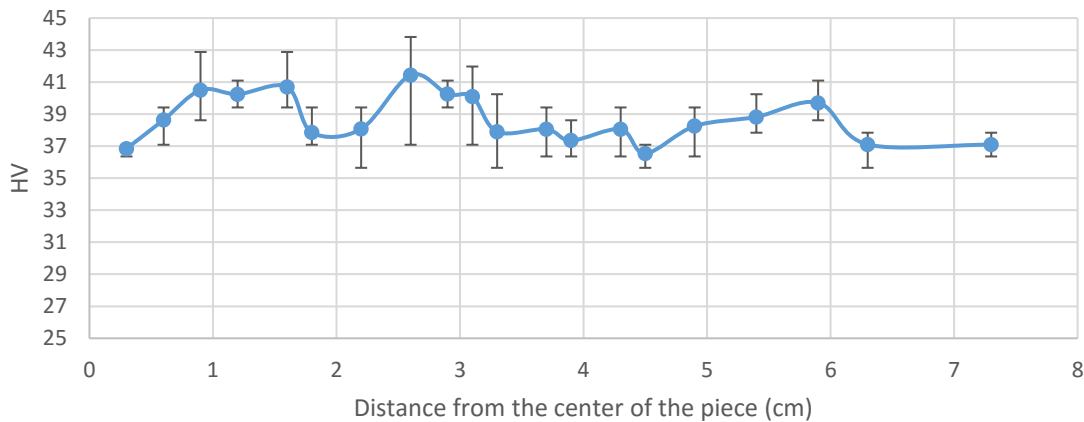
Figure 61: Evolution of the microhardness value with the distance from the center of the AA1050 piece.

Similarly to that observed for the strain, fluctuation of experimental values the microhardeness can be seen in Figure 58. This supports the previous hypothesis that the deformation of the piece during

the SPIF process is not homogeneous and justify a posteriori the selection of microhardness tests to characterize the mechanical behavior of the material after SPIF instead of other type of tests, such as tensile tests (used to characterize the initial materials).

4.2.1.3. Crystallographic Texture Characterization

Figure *62* shows the {1 0 0} and {1 1 1} pole figures after SPIF process. No major change in the crystallographic texture is seen from the comparison of these pole figures and the ones obtained in the as-received AA1050. It is worth to say that additional crystallographic textures measurements in different thickness planes also did not show significant changes in the crystallographic orientations of the aluminum grains.
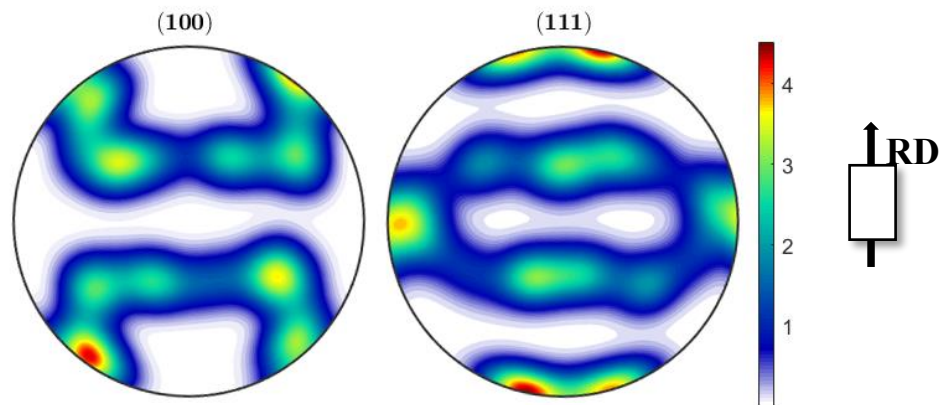
Figure 62: Experimental {1 0 0} and {1 1 1} pole figures of AA1050 after SPIF process (zone near from the center of the piece).

4.2.1.4. Microstructure Characterization

Figure 63 shows a TEM image obtained near from the center of the piece of AA1050 produced by SPIF. Comparing with the images of as-received aluminum (Figure 39), there is no major microstructural differences. Indeed the microstructure of both are characterized by presence

of sub-grains with similar size and shape. This conclusion is reinforced by the comparison of EBSD maps before (Figure 40) and after (Figure 64) SPIF deformation where it is possible to identify for both cases, large regions which are preferentially oriented in rolling direction and the sub-grain structure. These results show that both initial rolling microstructure and crystallographic texture of AA1050 are very stable and do not evolve significantly during the SPIF deformation.
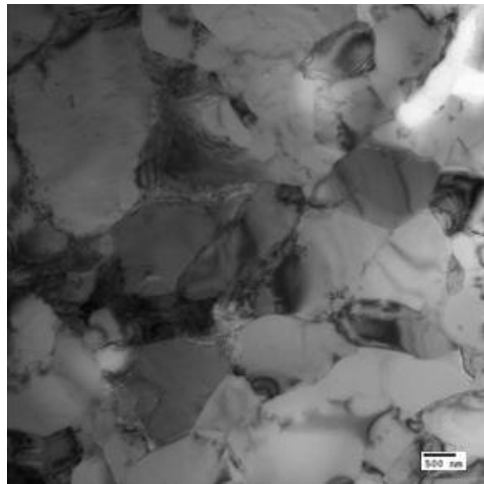
Figure 63: TEM image of AA1050 after SPIF process (zone near from the center of the piece).
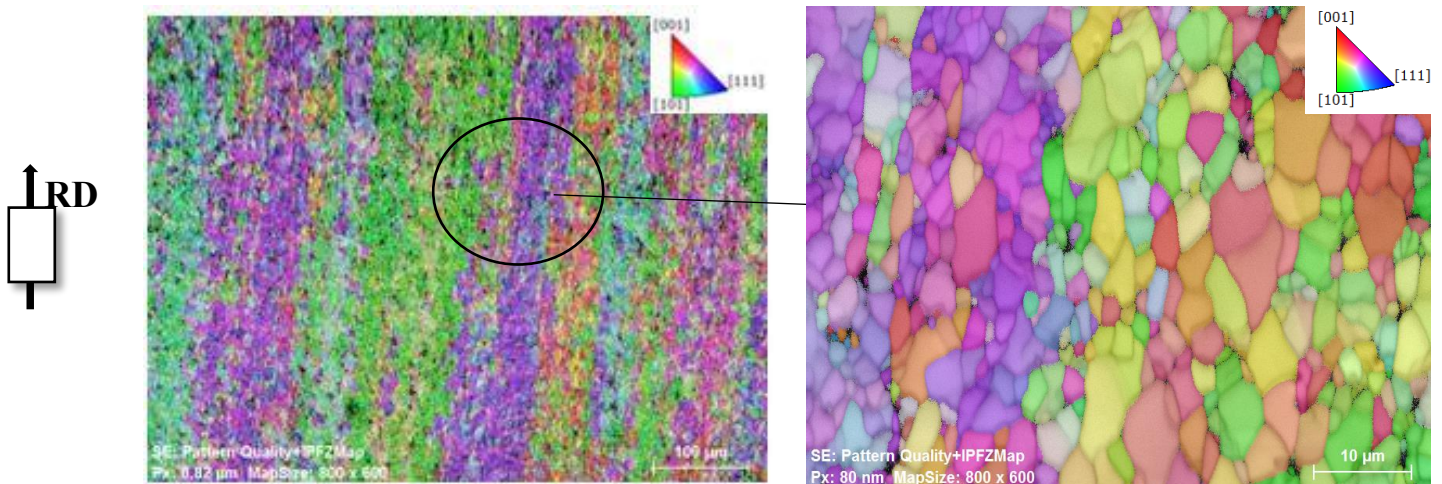
Figure 64: Crystallographic orientation EBSD maps obtained on AA1050 after SPIF.

4.2.2. Low Carbon Steel

4.2.2.1. Strain and Thickness Measurement

In Figure 65 is presented the evolution of the experimental true strain values measured in LC steel and the values calculated from eqns. 15 and 33, with the distance from the center of the piece. The experimentally measured thickness is compared with the calculated values from eqn. 32 in Figure 66.
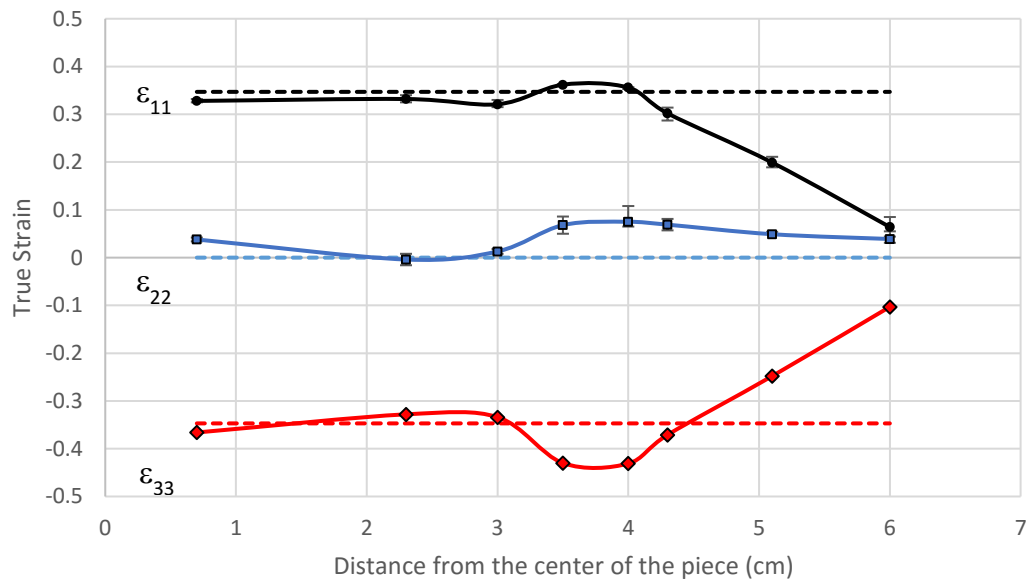
Figure 65: Evolution of the experimental values of ε_{11} and ε_{22} (continuous black and blue lines, respectively) and ε_{33} calculated (continuous red line) from equation 15, with the distance from the center for the LC steel piece. The non-continuous lines represent the strain values calculated from equation 33.
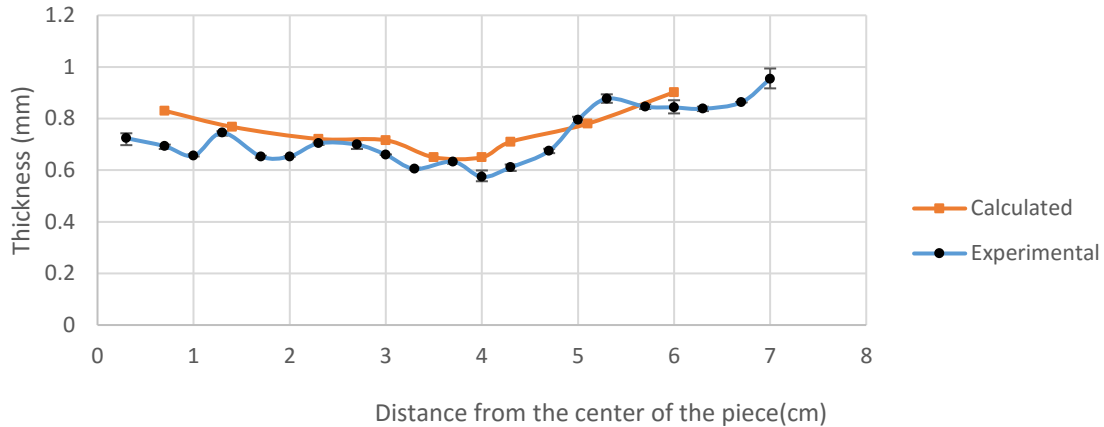
Figure 66: A comparison between the theoretical and experimental thickness for LC steel.

Comparing the Figure 65 and Figure 66 with Figure 59 and Figure 60, similar observations can be made with respect to the trend of the curves. Indeed, it can be seen good agreements between experimental strain values measure near from the center of the piece and values predicted from the sin law (Figure 65) and between experimental and calculated thickness (Figure 66). However, comparing with AA1050 sheet, the behavior shown by the LC steel show a less marked fluctuation of the strain values and a smaller distance from the center of the piece after which the experimental strain diverge from the values predicted by the sin law. These differences suggest that the deformation of the LC steel promoted by the SPIF tool is less localized than for AA1050 sheet, due to the higher flow stress of the steel.

4.2.2.2. Microhardness Measurements

In Figure 67 is presented the evolution of the microhardness along the deformed LC steel. Unlike aluminum, there is an increase of hardness with the decrease of the distance to the center of the piece. This shows that, due to the low initial hardening state of the LC steel, the increase of hardening due to the deformation promoted by the SPIF tool is enough to be detected by microhardness tests.
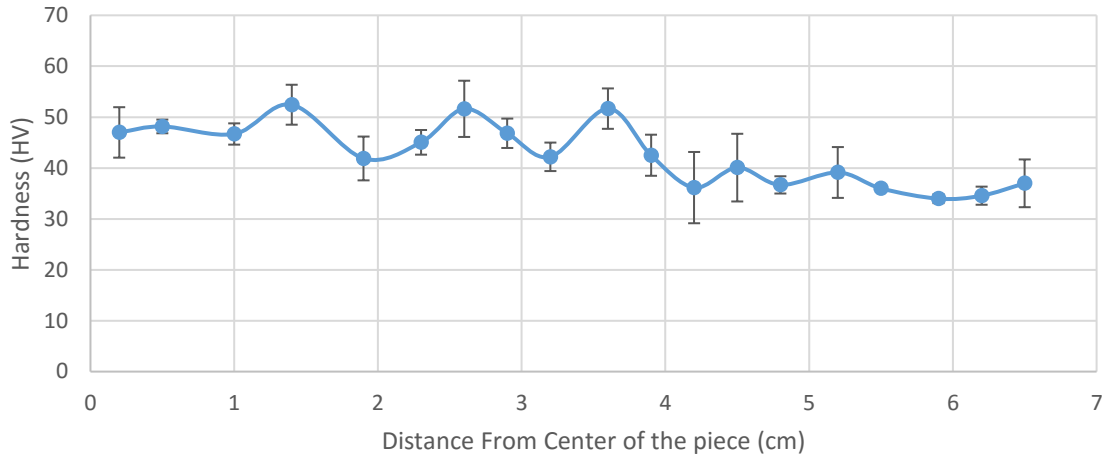
Figure 67: Evolution of the microhardness value with the distance from the center of the LC piece.

4.2.2.3. Crystallographic Texture Characterization

Figure 68 shows the {1 0 0} and {1 1 0} pole figures of LC steel after SPIF process. As for AA1050, no major change in the crystallographic texture is seen from the comparison of these pole figures and the ones obtained in the as-received material.
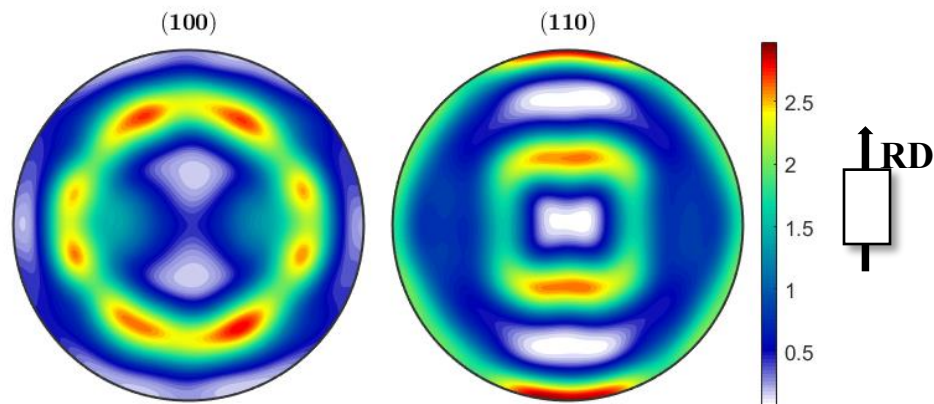
Figure 68: Experimental {1 0 0} and {1 1 0} pole figures of LC steel after SPIF process (zone near from the center of the piece).

4.2.2.4. Microstructure Characterization

TEM observations performed in LC steel deformed by SPIF showed a strong increase of the dislocation density, when compared with the as-received material. The resulting dislocation structure are characterized by the presence of equiaxed dislocation cells with approximately 1 μm (Figure 69) and walls less defined than in the AA1050.
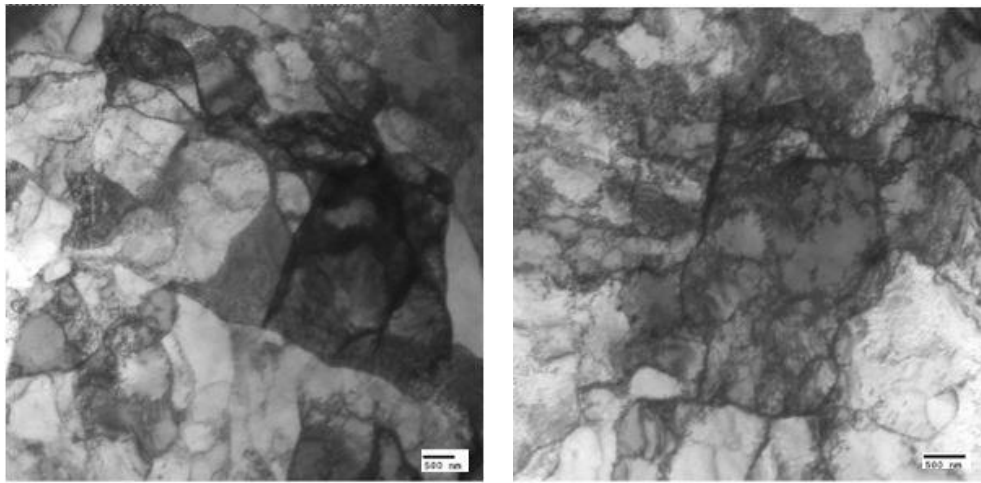
Figure 69: TEM micrograph of LC steel after deformation.

Additional information about the effect of the SPIF deformation on the microstructure can be extracted from the analysis of the EBSD analysis performed on the LC steel pieces (Figure 70 and Figure 71). Indeed, the comparison of the misorientation maps obtained from the EBSD maps of LC steel before and after SPIF (Figure 71) show significant differences in the homogeneity of the strain distribution inside each grain. More specifically, in the as-received material all points of each ferrite grains show similar crystallographic orientation and only low misorientation angles are measured. However, after the SPIF deformation, higher misorientation angles are observed in the LC steel, usually in the grain boundary regions. This heterogeneous deformation of the ferrite grains is a result of accommodation process of strain incompatibilities between neighbor ferrite grains.
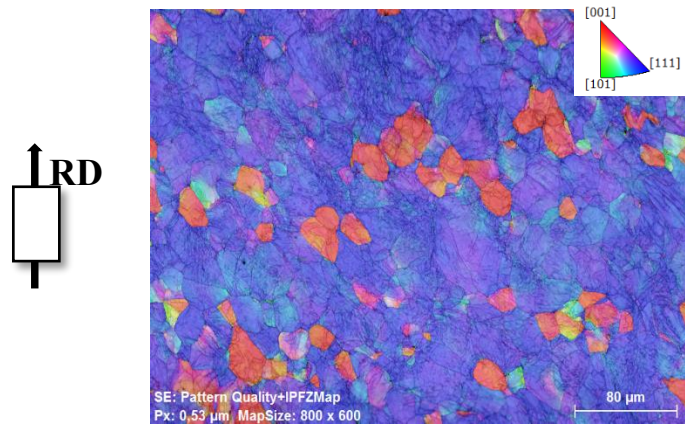
Figure 70: Crystallographic orientation EBSD maps obtained on LC steel after SPIF.

(a)

(b)

(c)

(d)
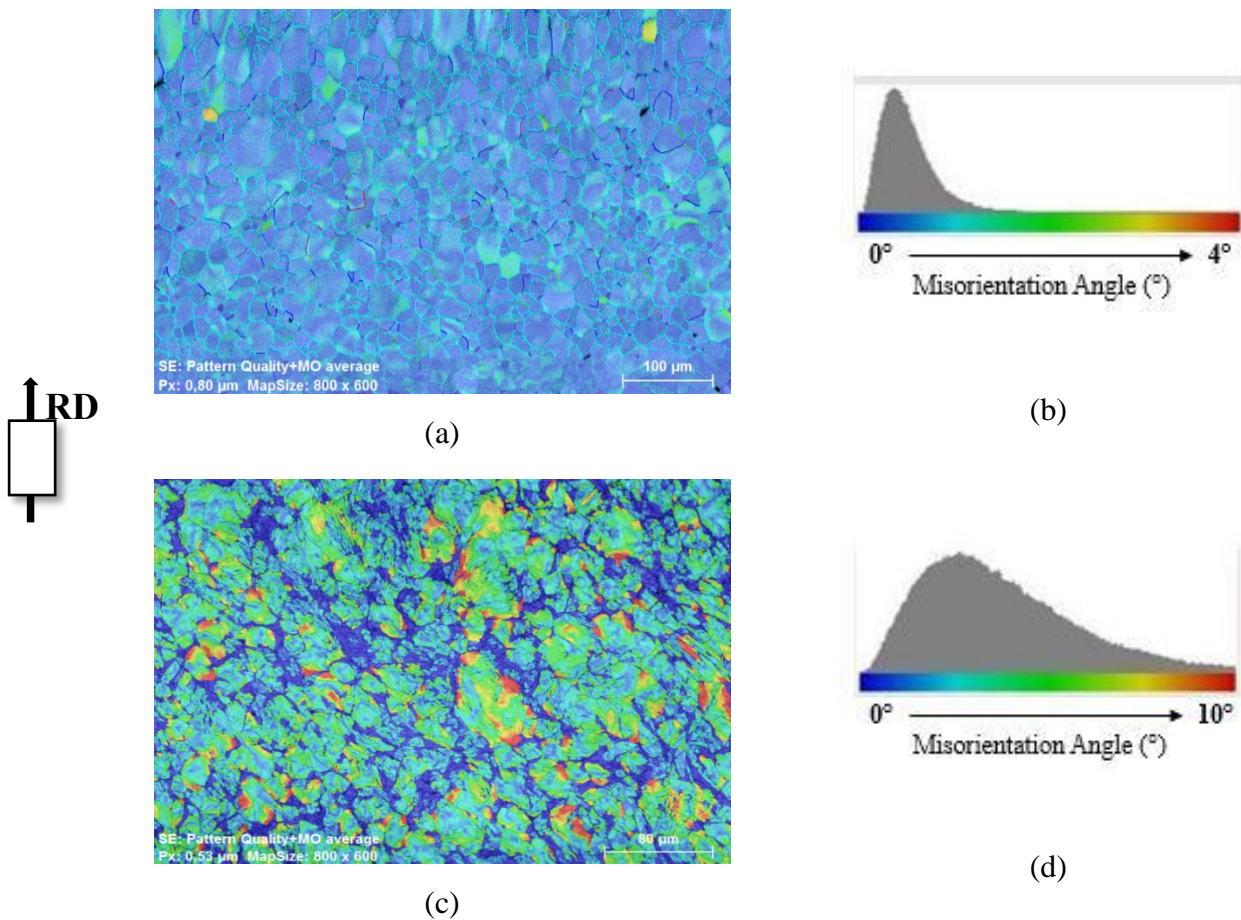
Figure 71: Misorientation maps of as-received (a) and after SPIF deformation (c) of LC steel. In (b) and (d) are presented misorientation angle frequency distribution before (b) and after (d) deformation.

4.2.3. Dual Phase Steel

4.2.3.1. Strain and Thickness Measurements

The evolution of the experimentally measured true strains in deformed DP780 piece is compared with the calculated values Figure 72 and Figure 73.
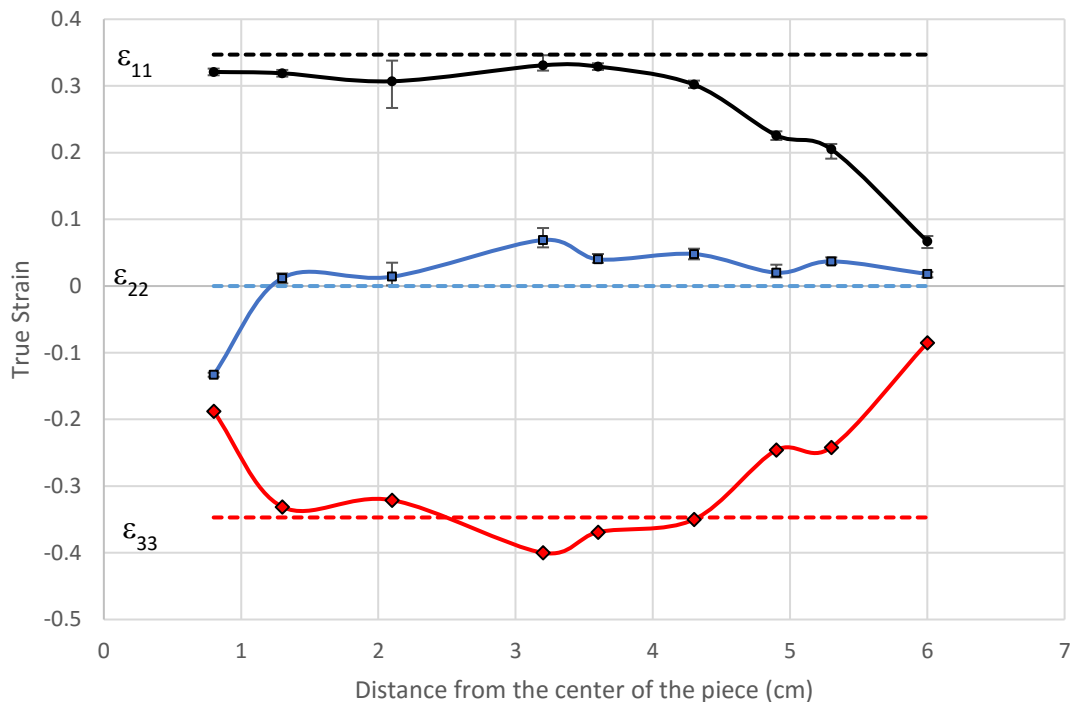
Figure 72: Evolution of the experimental values of ε_{11} and ε_{22} (continuous black and blue lines, respectively) and ε_{33} calculated (continuous red line) from equation 15, with the distance from the center for the DP780 steel piece. The non-continuous lines represent the strain values calculated from equation 33.

The same trend observed for AA1050 and LC steel is also observed for DP780 sheet. Although a good general agreement between the values measured and predicted by sin law values, significant differences are observed for the first point of the graph which can be explained by an additional deformation of the piece during the water jet cutting performed before the measurements. Also as

expected, taking into account the highest flow stress showed by the DP780 sheet, it is observed a less marked fluctuation of the strain values and decrease of the distance after which the experimental strain diverge from the values predicted by the sin law.
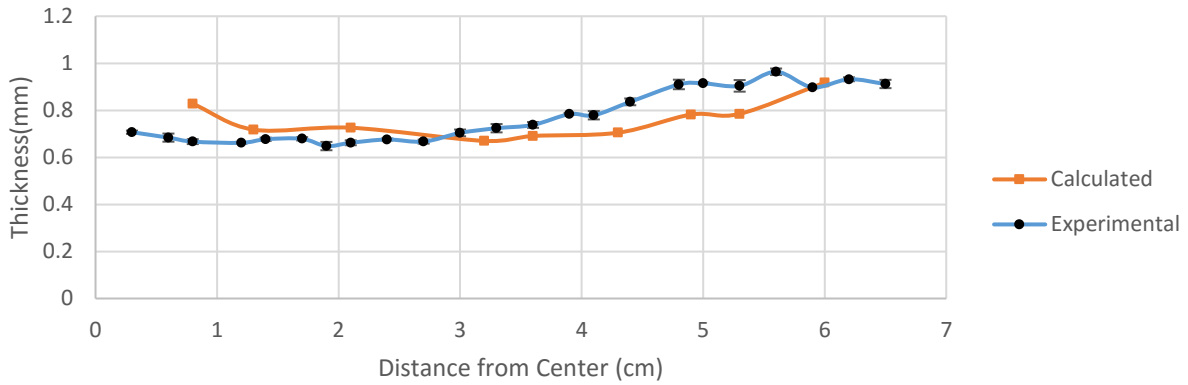
Figure 73: A comparison between the theoretical and experimental thickness for DP steel.

Another interesting comparison is the between thickness of clamped zone before and after SPIF (Figure 74). Assuming that the compressive forces applied by the clamp during SPIF is the same for all materials, the thickness reduction is, as suggested before, related with flow stress of the as-received materials.
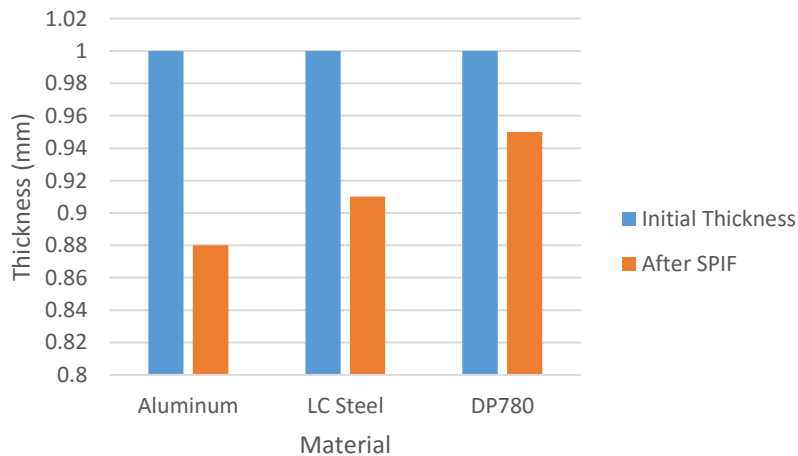
Figure 74: Thickness in the undeformed zone before and after SPIF.

4.2.3.2. Microhardness measurements

Figure 75 shows the microhardness measured for DP780 after deformation. Compared to aluminum and LC steel, the DP780 steel shows higher hardness values, as expected taking into account the presence of a relative large fraction of martensite in this material. Moreover, the hardness shows a decreasing trend as we move away from the center, confirming the strain gradient experimentally measured. The higher dispersion of the experimental values is attributed to the heterogeneous distribution of the martensite phase.
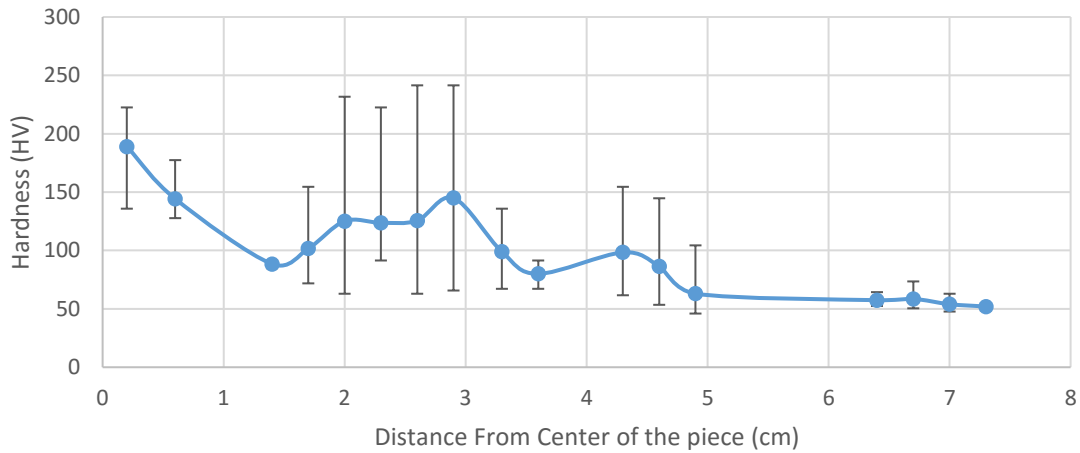
Figure 75: Evolution of the microhardness value with the distance from the center of the DP780 piece.

4.2.3.3. Crystallographic Texture Characterization

Figure 76 shows the experimental {1 0 0} and {1 1 0} pole figures of DP780 after SPIF process. As for the other materials, no noticeable change in texture is seen between before and after SPIF deformation.
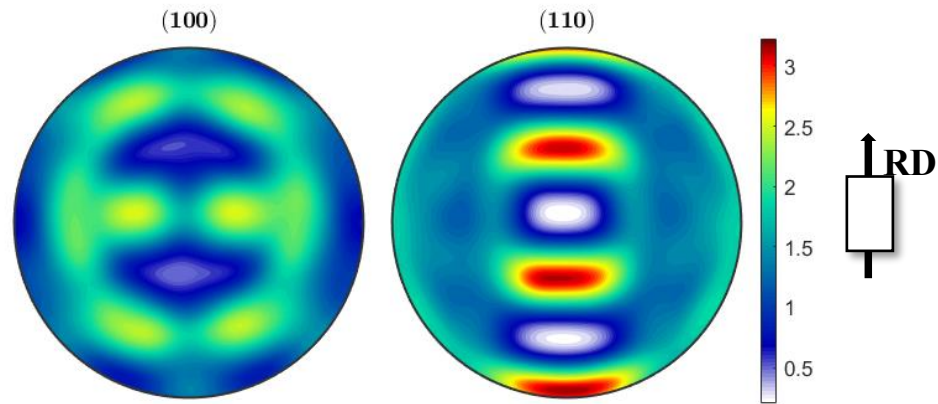
Figure 76: Experimental {1 0 0} and {1 1 0} pole figures of DP780 after SPIF process (zone near from the center of the piece).

4.2.3.4. Microstructure Characterization

TEM images obtained on deformed DP780 steel are presented in Figure 77. Comparing with the microstructure of the initial DP780 steel sheet, a strong increase on the dislocation density is seen.
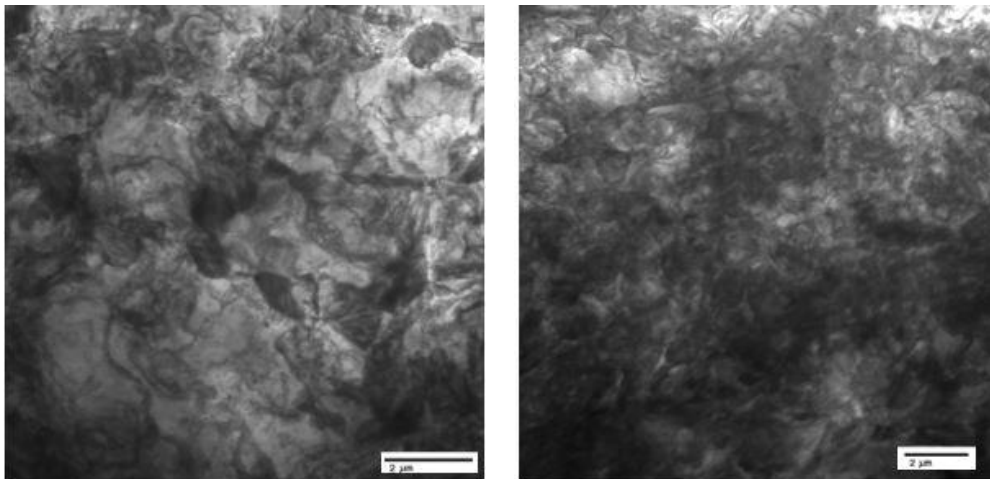
Figure 77: TEM micrograph of DP780 after deformation.

Comparing these results with images obtained on LC steel after the same forming conditions, it is noted also a significant increase in the dislocation density, which is justified by the increase of strain in ferrite grains due to the presence of relatively large fraction of undeformable material (around 35% of volume fraction of martensite), as discussed in section 4.1.3.1. It is likely that some strain accommodation incompatibilities between the ferrite and martensite particles can contribute also for an increase of plastic strain in ferrite grains near the grain boundaries. These strain incompatibilities between ferrite-ferrite and martensite-ferrite grains allows to explain the high misorientation angles observed near the grain boundaries (where most of the martensite particles are usually located) and the strong broadening of the frequency curve for higher misorientation angles observed on DP780 steel (Figure 76).
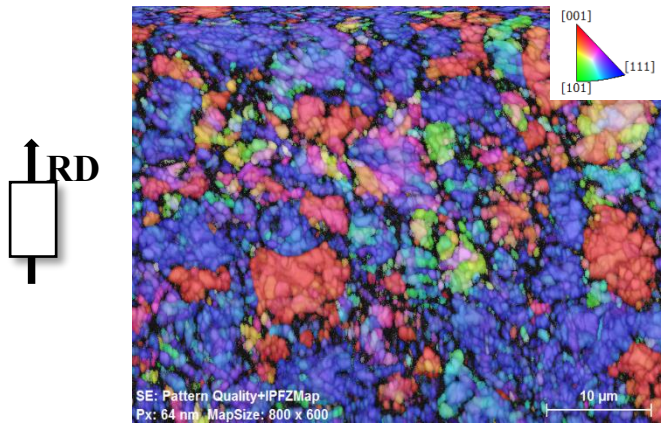
Figure 78: Crystallographic orientation EBSD maps obtained on DP780 after SPIF.

(a)

(b)

RD
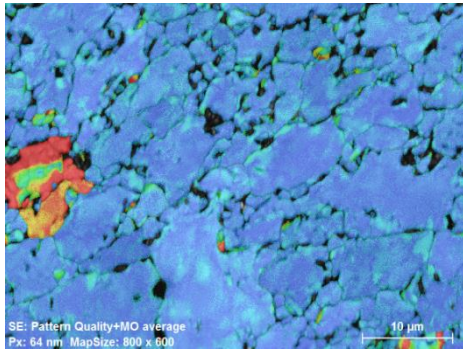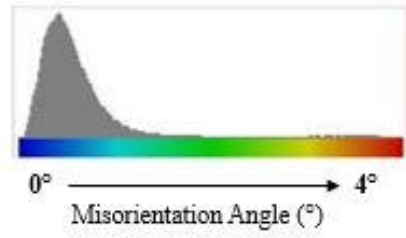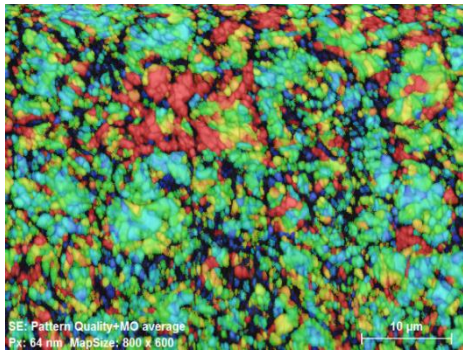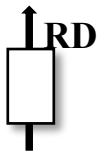
(c)
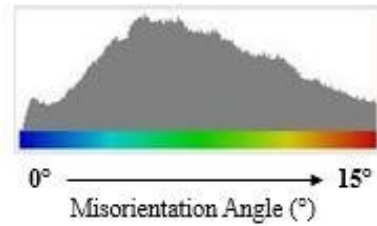
(d)

Figure 79: Misorientation maps of as-received (a) and after SPIF deformation (c) of DP780 steel. In (b) and (d) are presented misorientation angle frequency distribution before (b) and after (d) deformation.

5. Conclusions

5.1. Initial Materials

1. The AA1050 sheet shows a high yield stress and very low uniform strain values in tensile tests, indicating that the material was supplied in a hardened state. This was further confirmed by the crystallographic texture analysis, which revealed a typical crystallographic texture of rolled aluminum, and by TEM observations that show a sub-grains dislocation structure in the as-received material;

2. The analysis of tensile test curves and the VPSC model results showed that crystallographic texture of AA1050 was not the major influencing factor on the observed anisotropic behavior. For this material, the mechanical behavior can be explained based on the initial dislocation microstructure of the as-received material;

3. The anisotropic behavior of LC and DP780 steels were successfully predicted by the VPSC model, strongly suggesting that it has a crystallographic texture origin;

4. The microstructure of the as-received DP780 steel sheet is characterized by the presence of ferrite grains with around 30 μm and martensite particles, usually located in the grain boundaries. The measured volume fraction of martensite was around 35%;

5. The DP780 steel showed higher values of flow stress and a lower uniform strain, compared to LC steel. These differences were explained by the presence of martensite particles.

5.2. After SPIF

1. For all materials, a good agreement was observed between the thickness near the center of the piece produced by SPIF and the value predicted by the sin law (equation 1);

2. In spite of the very low uniform tensile strain value presented by the AA1050 sheet, it was possible to produce by SPIF a piece with the defined shape.

3. The deformation promoted by the SPIF tool decreased near the clamped area of the sheet, suggesting that different deformation modes are imposed to the piece during the initial and later stages of the SPI process;

4. There was a reduction of thickness in the clamped zone of the pieces as a result of the compressive forces induced by the clamping system;

5. Both the strain measurements and the microhardness tests showed a heterogeneous deformation of the pieces produced by SPIF. This was attributed to the localized plastic deformation promoted by the SPIF tool;

6. No significant change in the crystallographic texture or in the microstructure of AA1050 sheet before and after SPIF was observed, showing that the initial rolling microstructure and the crystallographic texture are very stable during the SPIF process;

7. There was no major change in the crystallographic texture during the SPIF deformation in both LC and DP780 steels. However, the TEM observations showed a strong increase of dislocation density and the development of equiaxed dislocation cell structure in both materials;

8. EBSD analysis showed a heterogeneous distribution of the strain along the ferrite grains in the two steels. More specifically, an increase of the misorientation angles was observed in both materials, usually near the grains boundaries. This misorientation between different regions of the ferrite grains is higher for DP780 and put in evidence the occurrence of strain accommodation process between neighbor ferrite grains and, in case of the DP780 steel, also between ferrite grains and the martensite particles.

6. Proposals for Future Work

Based on the results achieved in this study, it is proposed for future work a study of the evolution of crystallographic texture and dislocation microstructure along the process, rather than after the end of process, to understand more about the physical mechanisms involved in the plastic deformation at each instant of the SPIF process. Also, should be analyzed the influence of different processing parameters, such as tool size and step size, feed rate, etc. The results from this study would be used in finite element simulations code in order to predict the behavior of the material during the SPIF process and to select the optimized conditions to produce a specific product.

References

Abbaschian, R., Reed-Hill, R.E., (2008). Physical Metallurgy Principles. 4. Cengage Learning.

Allwood, J. M, Shouler, D. R., and Tekkaya, A. E., (2007). "The increased forming limits of incremental sheet forming processes." Key Engineering Materials, July: pp 621-628. doi:10.4028/www.scientific.net/KEM.344.621.

Allwood, J. M., King, G., Duflou, J. R., (2004). "Structured Search for Applications of the Incremental Sheet Forming Process by Product Segmentation." IMECH E, Proceedings Part B, Journal of Engineering and Manufacture 219: pp 239-244.

Ambrogio G., Filice, L., Manco, G.L., (2008). "Warm incremental forming of magnesium alloy AZ31." CIRP Annals - Manufacturing Technology 57 (1): pp 257-260. doi:10.1016/j.cirp.2008.03.066.

Ambrogio, G., Filice, L., Micari, F., (2006). "A force measuring based strategy for failure prevention in incremental forming." Journal of Materials Processing Technology 177 (1-3): pp 413-416. doi:10.1016/j.jmatprotec.2006.04.076.

Austin, R.A., McDowell, D.L., (2011). "A dislocation-based constitutive model for viscoplastic deformation of fcc metals at very high strain rates." International Journal of Plasticity 27 (1): pp 1-24. doi:10.1016/j.ijplas.2010.03.002.

Benedetti, M., Fontanari, V., Monelli, B., Tassan M., (2015). "Single-point incremental forming of sheet metals: Experimental study and numerical simulation." Journal of Engineering Manufacture (SAGE). doi:10.1177/0954405415612351.

Bergström, Y., Granbom Y., Sterkenburg, D., (2010). "A Dislocation-Based Theory for the Deformation Hardening Behavior of DP Steels: Impact of Martensite Content and Ferrite Grain Size." Journal of Metallurgy. doi:10.1155/2010/647198.

Bunge, H. J., Morris, P. R., (1982). Texture analysis in materials science: mathematical methods. London: Butterworths.

Dieter, G.E.,(1988). Mechanical Metallurgy. Edited by David Bacon. McGraw-Hill.

Duflou J., Tunckol, Y., Szekeres, A., Vanherck, P., (2007). "Experimental study on force measurements for single point incremental forming." Journal of Materials Processing Technology 189 (1-3): pp 65-72. doi:10.1016/j.jmatprotec.2007.01.005.

Duflou, J. R., Lauwers, B., Verbert, J., (2005). "Medical application of single point incremental forming: cranial plate manufacturing." Proceedings of the 2005VRAP Conference. Leiria. pp 161-164.

Duflou, J. R., Verbert, J., Belkassem, B., Henrard, C., (2008). "Multi-Step toolpath approach to overcome forming limitations in single point incremental forming." International Journal of Material Forming 1: pp 1203-1206. doi:10.1007/s12289-008-0157-2.

Dutta, S., (2011). "Influence of the strain path change on the mechanical behavior of Mg alloys." Master Thesis, Departamento de Engenharia Cerâmica e do Vidro, University of Aveiro, Aveiro, 76.

Echrif, A.B.M., Hrari, M., (2011). "Research and progress in incremental sheet forming processes." Materials and Manufacturing Processes 26 (11): pp 1401-1414.

Emmens, W. C., van den Boogaard, A. H., (2007). "Strain in shear and material behaviour in incremental forming." Key Engineering Materials 344: pp 519-526.

Engler, O., Randle, V., (2009). Introduction to Texture Analysis: Macrotexture, Microtexture, and Orientation Mapping. 2nd. CRC Press.

Fábio, J.P.M., (2008). "Asymmetrical rolling of an aluminum alloy 1050." PhD Thesis, Departamento de Engenharia Mecânica, University of Aveiro, Aveiro, 146.

Federici, C., Maggi, S., Rigoni, S., (2005). "The Use of Advanced High Strength Steel Sheets in the Automotive Industry." Fiat Auto Engineering & Design.

Filice, L., Fantini, L., Micari, F., (2002). "Analysis of Material Formability in Incremental Forming." Annals of the CIRP 51 (1): pp 199-202.

Franzen, V., Kwiatkowski, L., Martins, P.A.F., Tekkaya, A.E., (2009). "Single point incremental forming of PVC." Journal of Materials Processing Technology 209: pp 462-469.

Fratini, L, Ambrogio, G, Di Lorenzo, R, Filice, L, Micari, F., (2004). "Influence of Mechanical Properties of the Sheet Material on Formability in Single Point Incremental Forming." Annals of CIRP 53 (1): pp 207-210.

Grassino, J., Vedani, M., Vimercati, G., Zanella, G., (2012). "Effects of skin pass rolling parameters on mechanical properties of steels." International Journal of Precision Engineering and Manufacturing 13 (11): pp 2017-2026. doi:10.1007/s12541-012-0266-1.

Hagan, E., and Jeswiet, J., (2004). "Analysis of surface roughness for parts formed by CNC incremental forming." IMECHE part B, J. of Engineering Manufacture 218 No. B10: pp 1307-1312.

Ham M, Jeswiet J.,(2007). "Forming limit curves in single point incremental forming." CIRP Annals Manufacturing Technology 56 (1): pp 277-280.

Ham, M., Jeswiet, J.,(2006). "Single point incremental forming and the forming criteria for AA3003." CIRP Annals Manufacturing Technology 55 (1): pp 241-244.

Hirt G., Junk, S., Witulski, N.,(2002). "Incremental Sheet Forming: Quality Evaluation and Process Simulation." 7th ICTP International Conference on Technology of Plasticity. Yokohama.

Hirt, G., Ames, J., Bambach, M., Kopp, R.,(2004). "Forming Strategies and Process Modelling for CNC incremental Sheet Forming." Annals of CIRP 53 (1): 203.

Hussain, G., Gao, L., Hayat, N., Xu. Ziran.,(2009). "A new formability indicator in single point incremental forming." Journal of Materials Processing Technology 209 (9): pp 4237-4242.

Jackson, K., Allwood, J.,(2009). "The mechanics of incremental sheet forming." Journal of Materials Processing Technology 209 (3): pp 1158-1174.

Jadhav, S., (2004). "Basic investigation of the incremental sheet metal forming process on a CNC milling machine." PhD Thesis, University of Dortmund, Dortmund.

Jesweit, J., Young, D., (2005). "Forming limit diagrams for single point incremental forming of aluminium sheet." Proc. ImechE, Part B: J. Engineering Manufacture 219: pp 359-364.

Jeswiet J., Hagan, E., (2001). "Rapid proto-typing of a headlight with sheet metal." Proceedings of ShemMet. pp 165-170.

Jeswiet, J., Micari, F., Hirt, G., Bramley, A., Duflou, J., Allwood, J., (2005). "Asymmetric Single Point Incremental Forming of Sheet Metal." CIRP Annals - Manufacturing Technology (Elsevier) 54 (2): pp 88-114. doi:10.1016/S0007-8506(07)60021-3.

Jiecen, Z., Hongshuang, D., Yonggang, D., Misra R.D.K., (2015). "Effect of martensite morphology and volume fraction on strain hardening and fracture behavior of martensite–ferrite dual phase steel." Materials Science and Engineering: A 627: 230-240.

Karaman, I., Sehitoglu, H., Beaudoin, A.J., Chumlyakov, Y.I., Maier, H.J., Tomé, C.N., (2000). "Modeling the deformation behavior of Hadfield steel single and polycrystals due to twinning and slip." Acta Materialia 48 (9): pp 2031-2047. doi:10.1016/S1359-6454(00)00051-3.

Keeler, S.P., Backofen, W.A., (1963). "Plastic instability and fracture in sheet stretched over rigid punches." Transaction of ASM 56: pp 25-48.

Kim, T. J., Yang, D. Y., (2000). "Improvement of formability for the incremental sheet metal forming process." International Journal of Mechanical Sciences 42 (7): pp 1271-1286. doi:10.1016/S0020-7403(99)00047-8.

Kim, Y. H., Park, J. J., (2002). "Effect of process parameters on formability in incremental forming of sheet metal." Journal of Materials Processing Technology 130-131: pp 42-46. doi:10.1016/S0924-0136(02)00788-4.

Kitazawa, K., (1997). "Limit strains for CNC incremental stretchexpanding of aluminum sheets." Journal of Japan Institute of Light Metals 47: pp 145-150.

Kudrathon, B., (2010). "Asymmetric rolling of aluminum 1050." Master Thesis, Departamento de Engenharia Cerâmica e do Vidro, University of Aveiro, Aveiro, 65.

Kuhlmann-Wilsdorf, D., (1989). "Theory of plastic deformation: - properties of low energy dislocation structures." Materials Science and Engineering: A 113 (1): pp 1-41. doi:10.1016/0921-5093(89)90290-6.

Kumar, Y., Kumar, S., (2015). "Advances in Material Forming and Joining." In Topics in Mining, Metallurgy and Materials Engineering, edited by R.G. Narayanan and U.S. Dixit. Springer India. doi:10.1007/978-81-322-2355-9_2.

Leach, D., Green, A.J., Bramley, A.N., (2001). "A new incremental sheet forming process for small batch and prototype parts." Proceedings of the 9th International Conference on Sheet Metal. Leuven. pp 211-218.

Lebensohn, R. A, Tomé, C. N., (1993). "A self-consistent anisotropic approach forthe simulation of plastic deformation and texture development of polycrystals:Application to zirconium alloys." Acta Metallurgica et Materialia 41 (9): pp 2611-2624.

Lebensohn, R. A., Tome, C. N., (1994). "A self-consistent viscoplastic model: prediction of rolling textures of anisotropic polycrystals." Materials Science and Engineering A 175 (1-2): pp 71-82.

Leszak, E., (1967). Apparatus and Process for Incremental Dieless Forming. Patent US3342051A1. 09 19.

Lopes, A. L. B., (2001). "Análise microestrutural das instabilidades plásticas em materiais metálicos." PhD Thesis, Departamento de Engenharia de Materiais e Cerâmica, University of Aveiro, Aveiro, 227.

Marciniak, Z., (1965). "Stability of plasctic shells under tension with kinematic boundary conditions,." Archives of Mechanical 17: pp 577-592.

Martins, M.A.B.E., (2011). "Project and construction of a Single Point Incremental Forming Machine." Master Thesis, Department of Mechanical Engineering, Univeristy of Aveiro, Aveiro, 81.

Martins, P. A. F., Bay, N., Skjoedt, M., Silva, M. B., (2008). "Theory of single point incremental forming." CIRP Annals - Manufacturing Technology 57: pp 247-252.

Martins, P. A. F., Kwiatkowski, L., Franzen, V., Tekkaya, A.E., Kleiner, M., (2009). "Single point incremental forming of polymers." CIRP Annals - Manufacturing Technology 58: pp 229-232.

Meier, H., Buff, B., Laurischkat, R., Smukala, V., (2009). "Increasing the part accuracy in dieless robot-based incremental sheet metal forming." CIRP Annals - Manufacturing Technology 58 (1): pp 233-238. doi:10.1016/j.cirp.2009.03.056.

Micari, F., (2004). "A common shape for conducting incremental forming tests." Proceedings of the 1st Incremental Forming Workshop. Saarbrücken.

Milutinović, M., Lenđel, R., Potran, M., Vilotić, D.,Skakun, P., Plančak, M., (2014). "Application of Single Point Incremental Forming for Manufacturing of Denture Base." Journal for Technology of Plasticity 39 (2).

Molinari, A., Canova, G. R., Azhi, S., (1987). "A self-consistent approach of the large deformation polycrystal viscoplasticity." Acta Metallurgica 12: pp 2983-2994.

Müller, H., Enzmann, H., (1998). "Potentials of rapid prototyping techniques for the manufacture of prototype sheet metal techniques for the manufacture of prototype sheet metal." Proceedings of the European Conference on Rapid Prototyping and Manufacturing. pp 337-350.

Nakazima, K., T. Kikuma., (1967). "Forming limits under balanced biaxial stretching of steel sheets." Tetsu-to-Hagane 53 (4): pp 455-458.

Powell, N., Andrew, C., (1992). "Incremental forming of flanged sheet metal components without dedicated dies,." IMECHE part B, Journal of Engineering Manufacture 206: pp 41-47.

Rauch, E. F., (2004). "Effects of metal characteristics and experimental conditions on dislocation self-organization." Revue de Métallurgie 101 (12): pp 1007-1019. doi:10.1051/metal:2004106.

Sachs, G., (1928). "Zur Ableitung einer Fleissbedingung." Zeichschrift der Verein Deutscher Ingenieur 72: pp 734-736.

Schmid, E., (1924). Proceedings of the International Congress for Applied Mechanics. Deflt. pp 342.

Schmitt, J-H., Shen, E.L., Raphanel, J.L., (1994). "A parameter for measuring the magnitude of a change of strain path: Validation and comparison with experiments on low carbon steel." International Journal of Plasticity 10 (5): 535-551. doi:10.1016/0749-6419(94)90013-2.

Silva, M. B, Skjoedt, M., Atkins, A G., Bay, N., Martins, P A F., (2008). "Single-point incremental forming and formability—failure diagrams." The Journal of Strain Analysis for Engineering Design 43: pp 15-35.

Silva, M. B, Skjoedt, M., Martins, P.A.F., Bay, N., (2008). "Revisiting the fundamentals of single point incremental forming by means of membrane analysis." International Journal of Machine Tools and Manufacture 48 (1): pp 73-83. doi:10.1016/j.ijmachtools.2007.07.004.

Silva, M. B., Alves, L.M., Martins, P.A.F., (2010). "Single point incremental forming of PVC :Experimental findings and theoretical interpretation." EuropeanJournalofMechanicsA/Solids (Elsevier Masson) 29: pp 557-566.

Smallman, R. E., Green, D., (1964). "The dependence of rolling texture on stacking fault energy." Acta Metallurgica 12 (2): pp 145-154. doi:10.1016/0001-6160(64)90182-8.

Smallman, R. E., Ngan, A.H.W., (2007). Physical Metallurgy and Advanced Materials Engineering. Butterworth-Heinemann.

Suwas, S., Ray, R.K., (2014). Crystallographic Texture of Materials. Springer-Verlag London. doi:10.1007/978-1-4471-6314-5.

Taylor, G. I., (1938). "Plastic strain in metals." Journal of the Institute of Metals 62: pp 307-324.

Tisza, M., (2012). "General overview of sheet incremental forming." Journal of Achievements in Materials and Manufacturing Engineering 55 (1): pp 113-120.

Torrão, J.N.D., (2013). "Control and execution of incremental forming using parallel kinematics." Master Thesis, Department of Mechanical Engineering, University of Aveiro, Aveiro, 136.

Verbert, J., Belkassem, B., Henrard, C., Habraken, A. M., Gu, J., Sol, H., Lauwers, B., Duflou, J. R., (2008). "Multi-Step toolpath approach to overcome forming limitations in single point incremental forming." International Journal of Material Forming 1: pp 1203-1206.

Vieira, M. F., (1994). "Solicitações Sequenciais em Cobre Policristalino: Comportamento após Pré-deformação." Tese de Doutoramento, Faculdade de Engenharia, Universidade do Porto, Porto.

Vincze, G., (2007). "Investigation methodologies for metals used in forming process." PhD Thesis, Department of Mechanical Engineering, University of Aveiro., Aveiro.

Wagoner, R., (2002). "Fundamental aspects of springback in sheet metal forming." Edited by D. Yang et.al. Proceedings Numisheet 2002. pp 13-19.

WorldAutoSteel. 2014. Dual Phase (DP) Steels.

Zaoui, A., (1990). Physique et Mécanique de la Mise en Forme des Métaux. Edited by F. Moussy and P. Franciosi. Vol. Cap. VI.4. Paris: Press du CNRS.